

Goal-oriented Uncertainty Quantification for Inverse Problems via Variational Encoder-Decoder Networks

Babak Maboudi Afkham[†], Julianne Chung^{*}, and Matthias Chung^{*}

[†]DTU Compute, Department of Applied Mathematics and Computer Science, Technical University of Denmark, Lyngby, Denmark

^{*}Department of Mathematics, Emory University, Atlanta, GA 30322, USA

October 2, 2023

Abstract

In this work, we describe a new approach that uses variational encoder-decoder (VED) networks for efficient goal-oriented uncertainty quantification for inverse problems. Contrary to standard inverse problems, these approaches are *goal-oriented* in that the goal is to estimate some quantities of interest (QoI) that are functions of the solution of an inverse problem, rather than the solution itself. Moreover, we are interested in computing uncertainty metrics associated with the QoI, thus utilizing a Bayesian approach for inverse problems that incorporates the prediction operator and techniques for exploring the posterior. This may be particularly challenging, especially for nonlinear, possibly unknown, operators and nonstandard prior assumptions. We harness recent advances in machine learning, i.e., VED networks, to describe a data-driven approach to large-scale inverse problems. This enables a real-time goal-oriented uncertainty quantification for the QoI. One of the advantages of our approach is that we avoid the need to solve challenging inversion problems by training a network to approximate the mapping from observations to QoI. Another main benefit is that we enable uncertainty quantification for the QoI by leveraging probability distributions in the latent space. This allows us to efficiently generate QoI samples and circumvent complicated or even unknown forward models and prediction operators. Numerical results from medical tomography reconstruction and nonlinear hydraulic tomography demonstrate the potential and broad applicability of the approach.

Keywords: deep learning, regularization, encoder-decoder networks, uncertainty quantification, quantity of interest, hyperparameter selection

1 Introduction

Inverse problems arise in many scientific applications, and there has been a significant amount of research on the development of theory and computational methods for solving inverse problems. However, solving an inverse problem is often just one step in a multi-step process, where the solution of the inverse problem is a tool that is used for some end goal (e.g., predictions that are used for optimal design or control). Standard approaches for goal-oriented inverse problems first seek a solution to the inverse problem and, informed by this solution, subsequently compute quantities of interest (QoI). While in some cases, estimation of these QoI is the end goal, there are many scenarios where uncertainties for the QoI provide critical information, e.g., for further decision-making. In this work, we are interested in *goal-oriented uncertainty quantification* (go-UQ), which combines goal-oriented inverse problems with uncertainty quantification for the QoI. In particular, we provide an efficient end-to-end computational approach that can be used to directly estimate the QoI and their uncertainties.

Consider a *goal-oriented inverse problem* of the form

$$\begin{aligned}\mathbf{b} &= F(\mathbf{y}) + \mathbf{e}, \\ \mathbf{x} &= G(\mathbf{y}),\end{aligned}\tag{1}$$

where $\mathbf{b} \in \mathbb{R}^m$ contains the observations, $\mathbf{y} \in \mathbb{R}^n$ contains unknown true parameters (e.g., the true image or state parameters), $F : \mathbb{R}^n \rightarrow \mathbb{R}^m$ is the parameter to observable map, and $\mathbf{e} \in \mathbb{R}^m$ represents additive noise. In classical inverse problems, the goal is to compute approximations of the unknowns in \mathbf{y} , given observations \mathbf{b} and knowledge of the forward operator F , [24]. Here, we are interested in *goal-oriented* inverse problems (1) where we aim to estimate some QoI in $\mathbf{x} \in \mathbb{R}^q$ that may be determined by a *prediction operator* $G : \mathbb{R}^n \rightarrow \mathbb{R}^q$, mapping the unknown \mathbf{y} onto \mathbf{x} .

Some motivating examples of goal-oriented inverse problems include carbon sequestration [35], modeling transport of a contaminant in an urban environment [3], and detecting the locations of discontinuities in reconstructed CT images [2, 11]. In many applications, the prediction operator may be simply taking a maximum, minimum, average, or some combination of the unknown parameters in \mathbf{y} , [3, 13, 35, 48]. However, QoIs may also be related to \mathbf{y} by more complex mappings where the prediction operator may not be well-defined or may rely on expert opinion (e.g., manual classification or segmentation of images). Regardless, the QoI typically represents some low dimensional property of the unknown \mathbf{y} , i.e., $q \ll n$.

Goal-oriented inverse problems suffer from the same obstacles as classical inverse problems such as ill-posedness and large parameter dimensions. Further challenges arise when considering UQ for the QoI due to the additional prediction operator G . Recent works on goal-oriented inverse problems consider modifications of the inversion process or the data acquisition process to take into account the output QoI. For example, in goal-oriented inference, end goals (i.e., output QoI) are incorporated into the inference process thereby leading to efficient inference-for-prediction algorithms [35, 36]. These approaches rely on estimating the uncertainty of some predictive QoI based on the solution of an inverse problem. However, the main difference is that these approaches target the most relevant parameters for prediction (i.e., modifying the inference process to account for output quantities of interest), and we are interested in estimating uncertainties of the QoI as the end goal. Goal-oriented approaches have also been considered in the context of optimal approximations [48] and optimal design of experiments [3]. These approaches use the output QoI, which are often linear mappings of the unknowns, to inform dimensionality reduction techniques and experimental design (e.g., optimal placement of sensors) respectively.

Overview of contributions In this work, we provide a novel computational framework for directly estimating the QoI and their uncertainties, given observations. We assume that sample pairs $\{(\mathbf{b}^j, \mathbf{x}^j)\}_{j=1}^J$ of observations and QoI are readily available and use a supervised learning approach to train a *variational encoder-decoder* (VED) network to approximate the mapping from observations \mathbf{b} to QoI \mathbf{x} . This approach confers several advantages:

- We bypass the computationally challenging inversion process of estimating \mathbf{y} by establishing an end-to-end framework that maps the observations \mathbf{b} directly to the QoI \mathbf{x} . Although one could consider a two-step approach where a network is used to approximate the inversion process from \mathbf{b} to \mathbf{y} [34], followed by the QoI computation, there are significant challenges due to the potentially large number of unknowns in \mathbf{y} . Dimension reduction techniques have been considered, e.g., to train a deep neural network (DNN) to approximate the mapping from observation data to desired (e.g., regularization) parameters [1, 37]; however, these approaches do not allow for UQ of the QoI.
- By leveraging VED networks, we can perform efficient UQ of the QoI. More specifically, we use a VED network to create a mapping from the observation to some latent space, enforce a predetermined distribution on the unobserved latent variables, and then create a mapping from the latent space to the target data distribution (e.g., the QoI). The latter half of the VED defines a generating function that maps independent and identically distributed (i.i.d.) samples from the latent space variables to the QoI. Once the network is trained, UQ for the QoI can be performed very efficiently in an online

phase, via forward propagation of the observation \mathbf{b} through the VED, where the output of the VED is a set of samples that can be used for the statistical description of the QoI \mathbf{x} .

- One key advantage of our approach is that it is data-driven, in that training data are used to circumvent complicated or even unknown forward models and prediction operators. Most goal-oriented approaches use linear prediction operators G . Our approach is not restricted to and does not require knowledge of G (or the forward operator F).

An overview of the paper is as follows. In Section 2 we provide a brief description of the Bayesian formulation for goal-oriented inverse problems and describe some basics of VED networks for readers unfamiliar with these machine learning techniques. Then in Section 3, we describe various details about using VED networks for go-UQ for inverse problems. Numerical experiments provided in Section 4 illustrate the benefits of our approach for various example applications and goal-oriented problem setups. Conclusions are provided in Section 5.

2 Background

Recall that for goal-oriented inverse problems (1), the standard approach is to first estimate the unknowns in \mathbf{y} , given \mathbf{b} and F , and second to compute the QoI \mathbf{x} from \mathbf{y} . However, standard approaches often do not reveal the uncertainties in this estimation. A popular approach that enables quantification of uncertainties (on \mathbf{y} , \mathbf{x} , or both) is to provide a probabilistic formulation for (1). That is, in order to provide information about the accuracy or uncertainties of the estimate, we are motivated to consider inverse problems in the framework of Bayesian statistics. In Section 2.1, we review the Bayesian formulation of an inverse problem with particular emphasis on prediction for the goal-oriented problem. Then, in Section 2.2 we describe tools from machine learning and their use within the inverse problems community. In particular, we describe VED networks that will be used in Section 3 for go-UQ.

2.1 Bayesian inverse problem

In this section, we describe a statistical approach to solving inverse problems. This approach enables us to include uncertainties, e.g., in measurement, into our model. In addition, the statistical approach provides a natural method for incorporating our prior knowledge of the parameters. Contrary to deterministic inverse problems where the goal is to compute a point estimate, the solution of a Bayesian inverse problem is a random variable and thus has a distribution [5]. More specifically, in the statistical framework, all unknown values are modeled as random variables. Let B, X, Y , and E be random vectors representing the observational data, the QoI, the unknown state, and additive noise, respectively. Then, the Bayesian interpretation of (1) is given by

$$B = F(Y) + E, \tag{2}$$

$$X = G(Y). \tag{3}$$

Note that since Y and E are unknown, we represent their uncertainties with a probability distribution constructed from prior knowledge. In the following, assuming for simplicity of illustration that all densities exist, the solution to the inverse problem (2) is given by the posterior density function, conditioned on the observations \mathbf{b} , i.e.,

$$\pi_{\text{post}}(\mathbf{y} \mid \mathbf{b}) \propto \pi_{\text{like}}(\mathbf{b} \mid \mathbf{y}) \pi_{\text{prior}}(\mathbf{y}). \tag{4}$$

Since we are interested only in the distribution of the QoI X rather than those of the state parameters Y themselves, the posterior distribution is propagated through to the QoI X , i.e.,

$$X \mid B = G(Y \mid B). \tag{5}$$

In the context of goal-oriented inference problems, this is often referred to as the *posterior predictive*, [35]. The prediction is a random variable and, hence, is characterized by a distribution. We denote its density by

$\pi_{\text{pred}}(\mathbf{x} \mid \mathbf{b})$. Given a prior and some observation, samples from the posterior $Y \mid B$ can be passed through the prediction process, and the resulting samples can be used to describe the posterior predictive and provide uncertainties for the QoI.

In the special case where the parameter-to-observable map is linear $F(\mathbf{y}) = \mathbf{A}\mathbf{y}$, the noise E and the prior Y are Gaussian, i.e., $E \sim \mathcal{N}(\mathbf{0}, \mathbf{\Gamma}_{\text{noise}})$ and $Y \sim \mathcal{N}(\bar{\mathbf{y}}, \mathbf{\Gamma}_{\mathbf{y}})$ with $\mathbf{\Gamma}_{\text{noise}}$ and $\mathbf{\Gamma}_{\mathbf{y}}$ symmetric and positive definite covariance matrices, the posterior (4) is also a Gaussian and is given by $\mathcal{N}(\mathbf{y}_{\text{post}}, \mathbf{\Gamma}_{\text{post}})$ where

$$\mathbf{\Gamma}_{\text{post}} = (\mathbf{A}^\top \mathbf{\Gamma}_{\text{noise}}^{-1} \mathbf{A} + \mathbf{\Gamma}_{\mathbf{y}}^{-1})^{-1} \quad \text{and} \quad \mathbf{y}_{\text{post}} = \mathbf{\Gamma}_{\text{post}} (\mathbf{\Gamma}_{\mathbf{y}}^{-1} \bar{\mathbf{y}} + \mathbf{A}^\top \mathbf{\Gamma}_{\text{noise}}^{-1} \mathbf{b}). \quad (6)$$

If, additionally, the prediction operator is linear, i.e., $G(\mathbf{y}) = \mathbf{P}\mathbf{y}$ for appropriately sized matrix \mathbf{P} , then the posterior predictive (5) is also a Gaussian and is given by $\mathcal{N}(\mathbf{x}_{\text{pred}}, \mathbf{\Sigma}_{\text{pred}})$ where

$$\mathbf{x}_{\text{pred}} = \mathbf{P}\mathbf{y}_{\text{post}} \quad \text{and} \quad \mathbf{\Sigma}_{\text{pred}} = \mathbf{P}\mathbf{\Gamma}_{\text{post}}\mathbf{P}^\top. \quad (7)$$

In the linear setting, a computationally efficient inference-for-prediction method was described in [35] that exploits underlying balanced truncation model reduction for dimension reduction. The posterior predictive was also used for the goal-oriented optimal design of experiments in [3].

So far, we have described goal-oriented approaches, and for the special case described above, efficient tools have been developed for exploring the posterior predictive. In this work, we exploit VED networks for go-UQ, resulting in a data-driven approach that can exploit recent developments in machine learning, is generalizable, and works for complex and even unknown prediction operators.

2.2 Learning from data

Machine learning has become an important tool in the inverse problems community. In this section, we provide some background on neural networks and describe the training process, given some training data. We describe how these networks work by starting with a description of DNNs, then encoder-decoder networks, and finally variational encoder-decoder networks.

Let us begin with the assumption that there exists some target function $\bar{\Phi} : \mathbb{R}^m \rightarrow \mathbb{R}^q$ that maps input vector $\mathbf{b} \in \mathbb{R}^m$ to a target output vector $\mathbf{x} \in \mathbb{R}^q$.

Deep neural networks (DNNs) *Deep feed-forward networks* or *deep neural networks* (DNNs) are among the many classic machine learning modeling tools. These networks are comprised of a composition of multiple layers of computation. In a feed-forward network, the layers together with their connections are typically represented by a directed graph, indicating the flow of information from the input to the target.

For simplicity, consider a feed-forward DNN with K layers for an input vector $\mathbf{b} \in \mathbb{R}^m$ and a target output vector $\mathbf{x} \in \mathbb{R}^q$ as

$$\Phi(\mathbf{b}; \boldsymbol{\theta}) = \varphi_{K+1}(\boldsymbol{\theta}_{K+1}) \circ \cdots \circ \varphi_1(\boldsymbol{\theta}_1)(\mathbf{b}) = \mathbf{x}, \quad (8)$$

where \mathbf{x} is the output of the network, \circ denotes the component-wise composition of functions $\varphi_k : \mathbb{R}^{r_{k-1}} \times \mathbb{R}^{p_k} \rightarrow \mathbb{R}^{r_k}$ for $k = 1, \dots, K+1$ ($r_0 = m$, and $r_{K+1} = q$). The vector $\boldsymbol{\theta} = [\boldsymbol{\theta}_1^\top, \dots, \boldsymbol{\theta}_{K+1}^\top]^\top \in \mathbb{R}^p$ is a composition of layer specific parameters $\boldsymbol{\theta}_k$ defining the so-called *weights* \mathbf{W}_k and *biases* \mathbf{d}_k , i.e., $\boldsymbol{\theta}_k = [\text{vec}(\mathbf{W}_k)^\top \quad \mathbf{d}_k^\top]^\top$, where $\mathbf{W}_k \in \mathbb{R}^{r_k \times r_{k-1}}$ and $\mathbf{d}_k \in \mathbb{R}^{r_k}$. The functions φ_k are given by

$$\mathbf{b}_k = \varphi_k(\boldsymbol{\theta}_k)(\mathbf{b}_{k-1}) = \mathbf{s}_k(\mathbf{W}_k \mathbf{b}_{k-1} + \mathbf{d}_k), \quad (9)$$

with $\mathbf{b}_0 = \mathbf{b}$ and where $\mathbf{s}_k : \mathbb{R}^{r_k} \rightarrow \mathbb{R}^{r_k}$ are typically nonlinear *activation functions*, mapping input arguments point-wise onto outputs with limiting range. Note that for the *output layer* $\varphi_{K+1}(\boldsymbol{\theta}_{K+1})$, we assume a linear transformation with no bias term, $\varphi_{K+1}(\boldsymbol{\theta}_{K+1})(\mathbf{b}_K) = \mathbf{W}_{K+1} \mathbf{b}_K$.

Given input-target pairs $\{(\mathbf{b}^j, \mathbf{x}^j)\}_{j=1}^J$, the aim of supervised learning is to train the neural network, i.e., computing network parameters $\boldsymbol{\theta}$, such that $\Phi(\mathbf{b}; \boldsymbol{\theta}) \approx \bar{\Phi}(\mathbf{b})$. For this, a *loss function* determines the

performance of a network by comparing $\Phi(\mathbf{b}^j; \boldsymbol{\theta})$ and \mathbf{x}^j for a particular $\boldsymbol{\theta}$. An optimization method is used to find appropriate network parameters $\boldsymbol{\theta}$ by minimizing a suitable loss function.

DNNs have been used for solving inverse problems (e.g., for regularization parameter selection [1, 37] or for learning regularization functionals [12, 23]). Furthermore, DNNs have been adopted for learning the inversion process, i.e., the mapping from the data space \mathbf{b} to the inverse solution \mathbf{y} , [34]. Such approaches could be extended for the prediction or estimation of the QoI.

Encoder-Decoder Networks DNNs can be implemented within an Encoder-Decoder (ED) architecture. Such networks consist of the concatenation of two networks (the encoder and the decoder). The encoder network is comprised of layers that successively reduce the dimension of the input vector. The output of the encoder is referred to as the *latent* vector $\mathbf{z} \in \mathbb{R}^\ell$ that describes a representation of the input. Then, the decoder network increases the dimension through the network to match the target dimension. More specifically, the two main parts can be defined using transformations:

- the encoder network $e : \mathbb{R}^m \times \mathbb{R}^{p^e} \rightarrow \mathbb{R}^\ell$ with network parameters $\boldsymbol{\theta}^e \in \mathbb{R}^{p^e}$ maps an input \mathbf{b} to the latent variables \mathbf{z} ,

$$\mathbf{z} = e(\mathbf{b}; \boldsymbol{\theta}^e), \quad (10)$$

- the decoder network $d : \mathbb{R}^\ell \times \mathbb{R}^{p^d} \rightarrow \mathbb{R}^q$ with network parameters $\boldsymbol{\theta}^d \in \mathbb{R}^{p^d}$ maps the latent variables to the output \mathbf{x} ,

$$\mathbf{x} = d(\mathbf{z}; \boldsymbol{\theta}^d). \quad (11)$$

The entire ED network then takes the form $\Phi_{\text{ed}}(\mathbf{b}; \boldsymbol{\theta}^e, \boldsymbol{\theta}^d) := d(e(\mathbf{b}; \boldsymbol{\theta}^e); \boldsymbol{\theta}^d)$. See Figure 1 for a visual representation of an ED network.

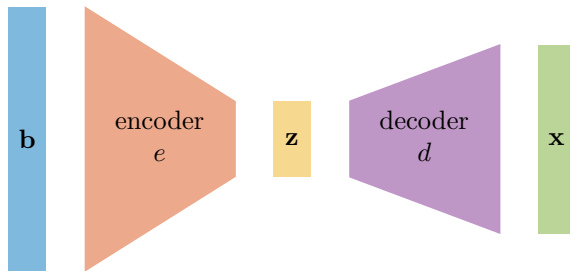


Figure 1: Encoder-decoder network mapping input vector \mathbf{b} to output vector \mathbf{x} . The encoder maps the input vector \mathbf{b} to the latent variables \mathbf{z} and the decoder maps the latent variables to the output \mathbf{x} .

Analogous to DNNs, the aim is to find parameters $\boldsymbol{\theta}^e$ and $\boldsymbol{\theta}^d$ that minimize some *loss function*. A common approach is to seek network parameters $\boldsymbol{\theta}^e, \boldsymbol{\theta}^d$ to minimize the mean squared error, i.e.,

$$\min_{\boldsymbol{\theta}^e, \boldsymbol{\theta}^d} \sum_{j=1}^J \left\| \mathbf{x}^j - \Phi_{\text{ed}}(\mathbf{b}^j; \boldsymbol{\theta}^e, \boldsymbol{\theta}^d) \right\|_2^2. \quad (12)$$

A commonly-used ED network is the *autoencoder*, which aims to map an input \mathbf{b} onto itself, i.e., $\Phi_{\text{ed}}(\mathbf{b}; \boldsymbol{\theta}^e, \boldsymbol{\theta}^d) \approx \mathbf{b}$. The encoder represents the input in a lower dimensional space while the decoder attempts to reconstruct the input from the low dimensional representation \mathbf{z} . The flow of data through a low-dimensional latent space forces the autoencoder to find a low-dimensional representation for a set of data, by which insignificant data is eliminated. Hence, such networks are classically used in dimensionality and noise reduction, and data compression applications, see e.g., [27, 47, 49, 52].

Variational Encoder-Decoder (VED) Networks Standard ED networks do not have *generative* capability, meaning a random sample from the latent space $\mathbf{z}^j \in \mathbb{R}^\ell$ may not necessarily generate a meaningful target sample $d(\mathbf{z}^j; \boldsymbol{\theta}^d)$. Variational Encoder-Decoder (VED) networks address this issue by enforcing a predetermined structure/distribution on the latent variables. This is particularly relevant in the context of variational autoencoders (VAEs), where the goal is to have the output match the input. Here, by sampling from the predetermined latent distribution, the decoder d provides a generating function that can be used to simulate or generate new data with desired features [29].

In a VED network, the input \mathbf{b} is passed through an encoder $e(\mathbf{b}; \boldsymbol{\theta}^e)$ that depends on parameters $\boldsymbol{\theta}^e$. This is similar to the ED networks where we reduce the dimensions of the input. However, the output of the encoder is a mean vector $\boldsymbol{\mu}^e \in \mathbb{R}^\ell$ and a vector of standard deviations $\boldsymbol{\sigma}^e \in \mathbb{R}^\ell$. For simplicity, we assume that $\boldsymbol{\mu}^e$ and $\boldsymbol{\sigma}^e$ define a Gaussian distribution for the latent vector \mathbf{z} , i.e.,

$$Z \sim \mathcal{N}(\boldsymbol{\mu}^e, \text{diag}(\boldsymbol{\sigma}^e)^2). \quad (13)$$

Then a sample \mathbf{z} is fed to the decoder $d(\mathbf{z}; \boldsymbol{\theta}^d)$ that depends on parameters $\boldsymbol{\theta}^d$. Notice that contrary to the ED network, the latent vector \mathbf{z} is not the output of the encoder but rather a sample from the latent distribution. See Figure 2 for a visual representation of a VED network.

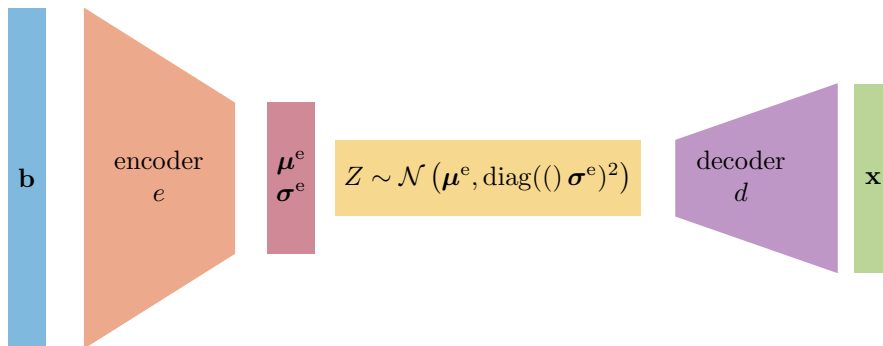


Figure 2: Variational Encoder-Decoder network mapping input vector \mathbf{b} to target vector \mathbf{x} . The encoder maps the input vector \mathbf{b} to the latent distribution defined by mean $\boldsymbol{\mu}^e$ and standard deviations $\boldsymbol{\sigma}^e$. The latent variables \mathbf{z} are obtained by sampling from the latent distribution, and the decoder maps the latent variables to the target \mathbf{x} .

Training a VED network requires determining network parameters $\boldsymbol{\theta}^e$ and $\boldsymbol{\theta}^d$ that minimize some objective or loss. However, contrary to DNNs and EDs, for VEDs there are two main components to consider. First, we wish to reconstruct an output matching a target by minimizing a training loss, e.g., for a sample $(\mathbf{b}^j, \mathbf{x}^j)$

$$\mathcal{D}_{\text{train}}^j(\boldsymbol{\theta}^e, \boldsymbol{\theta}^d) = \left\| \mathbf{x}^j - d(\mathbf{z}; \boldsymbol{\theta}^d) \right\|_2^2 \quad (14)$$

where

$$Z \sim \mathcal{N}(\boldsymbol{\mu}^e, \text{diag}(\boldsymbol{\sigma}^e)^2) \quad \text{with} \quad \begin{bmatrix} \boldsymbol{\mu}^e \\ \boldsymbol{\sigma}^e \end{bmatrix} = e(\mathbf{b}^j; \boldsymbol{\theta}^e). \quad (15)$$

Second, we aim to drive the latent space distribution toward the isotropic Gaussian (standard Gaussian with zero mean and unit variance), which can be obtained by minimizing a *similarity* loss between distributions. For example, we can define the similarity loss for the VED network as

$$\mathcal{D}_{\text{sim}}^j(\boldsymbol{\theta}^e) = \mathcal{D}_{\text{kl}}(\mathcal{N}(\boldsymbol{\mu}^e, \text{diag}(\boldsymbol{\sigma}^e)^2) \parallel \mathcal{N}(\mathbf{0}, \mathbf{I}_\ell)), \quad (16)$$

where \mathcal{D}_{kl} is the Kullback–Leibler (KL) divergence or KL loss [31], and the objective is to find encoder and

decoder parameters θ^e and θ^d that minimize the total loss [29],

$$\sum_{j=1}^J \mathcal{L}^j(\theta^e, \theta^d) \quad \text{where} \quad \mathcal{L}^j(\theta^e, \theta^d) = \mathcal{D}_{\text{train}}^j(\theta^e, \theta^d) + \mathcal{D}_{\text{sim}}^j(\theta^e). \quad (17)$$

Variational autoencoders are special cases of VED networks, and they have been used in various contexts for solving inverse problems, especially in imaging [4, 38, 41]. Variational autoencoders were also used in the context of uncertainty quantification in [18], where they were used to learn the parameter to observable map as well as the inverse problem solver. However, since the input and output dimensions must be the same for variational autoencoders and adversarial autoencoders, these approaches are too restrictive to be considered for goal-oriented UQ.

Another class of methods that combine learning from data with computational inverse problems is simulation based inference [10]. In these approaches, neural networks, which predict unknown parameters, are trained from a collection of simulated data. To incorporate uncertainties, deterministic neural networks are augmented with additional stochastic layers, e.g., see [17, 42, 43]. Although these methods show impressive performance in inferring model parameters, their evaluation of the predictive aspects of these parameters, e.g., the QoI, is lacking. This is particularly concerning for goal-oriented inverse problems, where the inverse map may be severely ill-conditioned.

3 Variational Encoder-Decoder (VED) networks for goal-oriented UQ

In this section, we describe an approach that builds a distribution on the QoI using a generative algorithm, which can be used to approximate the posterior predictive (5), where the distributions and mappings are encoded in the training data and its corresponding trained network. We establish a relationship between random variables B and X . The maps in this graph are approximated using a VED network. In Section 3.1, we argue how the relation between B and X results in a loss function similar to the one expressed in (17). We describe how training data can be used to estimate network parameters. Once the VED is trained and we have a new observation, we describe in Section 3.2 a sampling approach to perform UQ for the QoI.

Recall that the density function for the QoI $\pi(\mathbf{x})$ is, in general, unknown. We aim to approximate this distribution, as well as the density of the posterior predictive $\pi_{\text{pred}}(\mathbf{x} | \mathbf{b})$. In this approach, we assume there exists a latent variable with a convenient density function, e.g., a Gaussian density function, and consider a map $\bar{d}: \mathbb{R}^\ell \rightarrow \mathbb{R}^q$ such that $\mathbf{x} = \bar{d}(\mathbf{z})$. The benefit of such a map [33] is that it reduces the task of exploring an unknown and complex density function, e.g., $\pi(\mathbf{x})$, to exploring a computationally convenient density function. However, the complexity of $\pi(\mathbf{x})$ is still encoded in the nonlinear map \bar{d} .

We now relate $\pi(\mathbf{z})$ to the observation density $\pi(\mathbf{b})$ by introducing another map $\bar{e}: \mathbb{R}^m \rightarrow \mathbb{R}^\ell$, such that $\mathbf{z} = \bar{e}(\mathbf{b})$. Note that, in this case, the density function $\pi(\mathbf{b})$ is unknown. The composite map $\bar{d} \circ \bar{e}$ establishes a connection between B and X . We represent the connection between the random variables B , Z , and X in the graphical model in Figure 3.



Figure 3: Graphical model representing the connection between the observation \mathbf{b} , the latent variables \mathbf{z} and the QoI \mathbf{x} .

In the following, we assume that Z parameterizes X such that X and Z are indistinguishable to B , i.e.,

$$\pi(\mathbf{b} | \mathbf{x}, \mathbf{z}) = \pi(\mathbf{b} | \mathbf{z}) = \pi(\mathbf{b} | \mathbf{x}). \quad (18)$$

In other words, the parameterization of the prior distribution does not affect the data generation process. Now we check if the latent variable Z introduces a bias in the posterior predictive. We first construct an expression for the joint distribution,

$$\pi(\mathbf{b}, \mathbf{x}, \mathbf{z}) = \frac{\pi(\mathbf{b}, \mathbf{x})\pi(\mathbf{x}, \mathbf{z})}{\pi(\mathbf{x})} \quad (19)$$

since

$$\pi(\mathbf{b} | \mathbf{x}, \mathbf{z}) = \frac{\pi(\mathbf{b}, \mathbf{x}, \mathbf{z})}{\pi(\mathbf{x}, \mathbf{z})} \quad \text{and} \quad \pi(\mathbf{b} | \mathbf{x}) = \frac{\pi(\mathbf{b}, \mathbf{x})}{\pi(\mathbf{x})}. \quad (20)$$

Now we evaluate the bias in the posterior predictive in the presence of the latent variable \mathbf{z}

$$\pi(\mathbf{x} | \mathbf{b}, \mathbf{z}) = \frac{\pi(\mathbf{x}, \mathbf{b}, \mathbf{z})}{\pi(\mathbf{b}, \mathbf{z})} = \frac{\pi(\mathbf{b}, \mathbf{x})\pi(\mathbf{x}, \mathbf{z})}{\pi(\mathbf{x})\pi(\mathbf{b}, \mathbf{z})}, \quad (21)$$

where we used (19) in the last equality. Multiplying both the numerator and the denominator with $\pi(\mathbf{b})$ yields

$$\pi(\mathbf{x} | \mathbf{b}, \mathbf{z}) = \frac{\pi(\mathbf{b})}{\pi(\mathbf{b}, \mathbf{z})} \frac{\pi(\mathbf{x}, \mathbf{z})}{\pi(\mathbf{x})} \frac{\pi(\mathbf{b}, \mathbf{x})}{\pi(\mathbf{b})} = \frac{\pi(\mathbf{z} | \mathbf{x})}{\pi(\mathbf{z} | \mathbf{b})} \pi_{\text{pred}}(\mathbf{x} | \mathbf{b}). \quad (22)$$

Here we used the definition of a conditional distribution. Note that the right-hand side contains the posterior predictive $\pi_{\text{pred}}(\mathbf{x} | \mathbf{b})$, and the ratio $\pi(\mathbf{z} | \mathbf{x})/\pi(\mathbf{z} | \mathbf{b})$ does not equal to one for general maps \bar{d} and \bar{e} . However, we require \bar{d} and \bar{e} to satisfy the relation

$$\pi(\mathbf{z} | \mathbf{x}) = \pi(\mathbf{z} | \mathbf{b}). \quad (23)$$

In this case, the ratio in (22) is one, and $\pi(\mathbf{x} | \mathbf{b}, \mathbf{z})$ coincides with the posterior predictive.

3.1 Learning VED maps

In what follows, we discuss how to use training data to approximate maps \bar{e} and \bar{d} using VEDs. Assume that training data, $\{(\mathbf{b}^j, \mathbf{x}^j)\}_{j=1}^J$, containing observation and QoI pairs are provided. Let $e : \mathbb{R}^m \times \mathbb{R}^{p^e} \rightarrow \mathbb{R}^{2\ell}$ and $d : \mathbb{R}^\ell \times \mathbb{R}^{p^d} \rightarrow \mathbb{R}^q$ be an encoder and a decoder network, respectively.

In Figure 4, we provide a visual representation of the VED network used for goal-oriented UQ. The main distinction from the VED network in Figure 2 is that, in addition to enforcing a distribution on the latent variables, we assume a distribution on the target space so that we can perform UQ of the QoI.

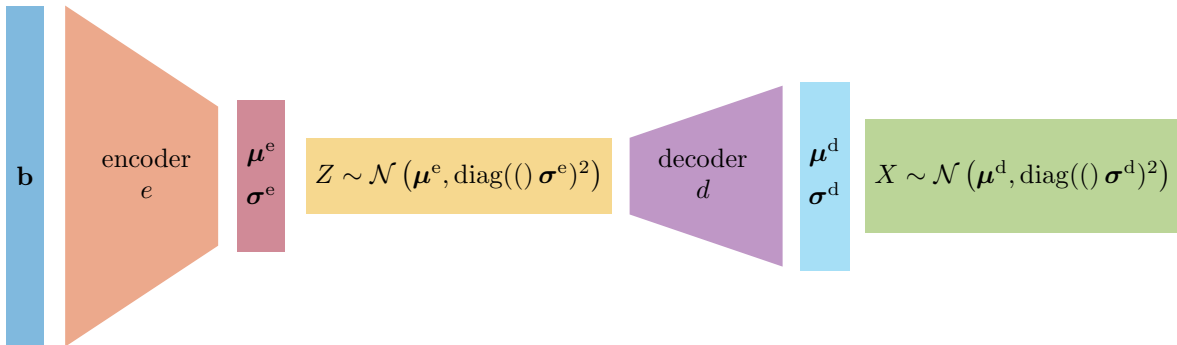


Figure 4: Variational encoder-decoder network mapping for goal-oriented UQ. The encoder maps the input vector \mathbf{b} to the latent variables \mathbf{z} and the decoder maps the latent variables to the target \mathbf{x} .

Ideally, we would like to obtain the equality in (23) with a learned encoder e and decoder d . Hence, we aim to learn the parameterized encoder and decoder to minimize the distance between both distributions

$\pi^e(\mathbf{z} \mid \mathbf{b})$ and $\pi^d(\mathbf{z} \mid \mathbf{x})$ in (23). We relax (23) to obtain the minimization problem

$$\min_{\theta^e, \theta^d} \mathcal{D}_{\text{kl}}(\pi^e(\mathbf{z} \mid \mathbf{b}) \parallel \pi^d(\mathbf{z} \mid \mathbf{x})). \quad (24)$$

Here, π^e is a family of distributions that the encoder e defines on the latent space. Similarly, π^d is a family of posterior distributions that are defined on the latent space. Therefore, the minimization problem (24) looks for the best approximation to (23) within these families. This approach is referred to as *variational inference* [19]. The superscript on a density function indicates the family to which the density function belongs.

We now expand (24) to obtain

$$\begin{aligned} \mathcal{D}_{\text{kl}}(\pi^e(\mathbf{z} \mid \mathbf{b}) \parallel \pi^d(\mathbf{z} \mid \mathbf{x})) &= \int_{\mathbb{R}^\ell} \pi^e(\mathbf{z} \mid \mathbf{b}) \log \left(\frac{\pi^e(\mathbf{z} \mid \mathbf{b})}{\pi^d(\mathbf{z} \mid \mathbf{x})} \right) d\mathbf{z} \\ &= \int_{\mathbb{R}^\ell} \pi^e(\mathbf{z} \mid \mathbf{b}) \log \left(\frac{\pi^e(\mathbf{z} \mid \mathbf{b})\pi(\mathbf{x})}{\pi^d(\mathbf{z}, \mathbf{x})} \right) d\mathbf{z} \\ &= \log(\pi(\mathbf{x})) \int_{\mathbb{R}^\ell} \pi^e(\mathbf{z} \mid \mathbf{b}) d\mathbf{z} + \int_{\mathbb{R}^\ell} \pi^e(\mathbf{z} \mid \mathbf{b}) \log \left(\frac{\pi^e(\mathbf{z} \mid \mathbf{b})}{\pi^d(\mathbf{z}, \mathbf{x})} \right) d\mathbf{z} \\ &= \log(\pi(\mathbf{x})) - \mathcal{L}(\theta^e, \theta^d). \end{aligned} \quad (25)$$

Here we used the definition of a conditional density in the second line, and the logarithm product rule in the third line. Moreover, $\mathcal{L}(\theta^e, \theta^d)$ is called the *evidence lower bound* (ELBO) [19] and is defined as

$$\mathcal{L}(\theta^e, \theta^d) = \int_{\mathbb{R}^\ell} \pi^e(\mathbf{z} \mid \mathbf{b}) \log \left(\frac{\pi^d(\mathbf{z}, \mathbf{x})}{\pi^e(\mathbf{z} \mid \mathbf{b})} \right) d\mathbf{z}. \quad (26)$$

Note that this is a lower bound on $\log(\pi(\mathbf{x}))$ since the KL divergence is non-negative. Following [29, 30], we want to differentiate and optimize the lower bound $\mathcal{L}(\theta^e, \theta^d)$, thus leading to

$$\max_{\theta^e, \theta^d} \mathcal{L}(\theta^e, \theta^d). \quad (27)$$

We now apply Bayes' theorem to (26) to obtain

$$\begin{aligned} \mathcal{L}(\theta^e, \theta^d) &= \int_{\mathbb{R}^\ell} \pi^e(\mathbf{z} \mid \mathbf{b}) \log \left(\frac{\pi^d(\mathbf{z}, \mathbf{x})}{\pi^e(\mathbf{z} \mid \mathbf{b})} \right) d\mathbf{z} \\ &= \int_{\mathbb{R}^\ell} \pi^e(\mathbf{z} \mid \mathbf{b}) \log \left(\frac{\pi^d(\mathbf{x} \mid \mathbf{z})\pi(\mathbf{z})}{\pi^e(\mathbf{z} \mid \mathbf{b})} \right) d\mathbf{z} \\ &= \int_{\mathbb{R}^\ell} \pi^e(\mathbf{z} \mid \mathbf{b}) \log(\pi^d(\mathbf{x} \mid \mathbf{z})) d\mathbf{z} + \int_{\mathbb{R}^\ell} \pi^e(\mathbf{z} \mid \mathbf{b}) \log \left(\frac{\pi(\mathbf{z})}{\pi^e(\mathbf{z} \mid \mathbf{b})} \right) d\mathbf{z} \\ &= \mathbb{E}_{\pi^e(\mathbf{z} \mid \mathbf{b})} \log(\pi^d(\mathbf{x} \mid \mathbf{z})) - \mathcal{D}_{\text{kl}}(\pi^e(\mathbf{z} \mid \mathbf{b}) \parallel \pi(\mathbf{z})). \end{aligned} \quad (28)$$

The first term in the right-hand-side of (28) is interpreted as computing an expectation with respect to the density function $\pi^e(\mathbf{z} \mid \mathbf{b})$. Note that the KL divergence in (24) is with respect to the posterior density $\pi^d(\mathbf{z} \mid \mathbf{x})$ while the one in (28) is with respect to the prior density $\pi(\mathbf{z})$.

Computing the ELBO, as expressed in (28), still poses challenges, e.g., density functions $\pi^e(\mathbf{z} \mid \mathbf{b})$ and $\pi^d(\mathbf{z} \mid \mathbf{x})$ are intractable for nonlinear maps e and d . We consider the following approximations to simplify the computation of the ELBO.

- (a) The prior density $\pi(\mathbf{z})$ is a standard normal density, i.e., following the distribution $\mathcal{N}(\mathbf{0}, \mathbf{I})$, with \mathbf{I} the identity matrix of size ℓ .
- (b) We assume that $\pi^e(\mathbf{z} \mid \mathbf{b})$ is a product of independent Gaussian densities, i.e.,

$$\pi^e(\mathbf{z} \mid \mathbf{b}) = \frac{1}{(2\pi)^{\ell/2} |\mathbf{D}^e(\mathbf{b})|} \exp \left(-\frac{1}{2} \|\mathbf{D}^e(\mathbf{b})^{-1}(\mathbf{z} - \boldsymbol{\mu}^e(\mathbf{b}))\|_2^2 \right), \quad (29)$$

where $\mathbf{D}^e(\mathbf{b}) = \text{diag}(\boldsymbol{\sigma}^e(\mathbf{b}))$ is a diagonal matrix and $|\cdot|$ denotes the determinant.

(c) We assume that $\pi^d(\mathbf{x} | \mathbf{z})$ is a product of independent Gaussian densities of the form

$$\pi^d(\mathbf{x} | \mathbf{z}) = \frac{1}{(2\pi)^{q/2} |\mathbf{D}^d(\mathbf{z})|} \exp\left(-\frac{1}{2} \|\mathbf{D}^d(\mathbf{z})^{-1}(\mathbf{x} - \boldsymbol{\mu}^d(\mathbf{z}))\|_2^2\right), \quad (30)$$

where $\mathbf{D}^d(\mathbf{z}) = \text{diag}(\boldsymbol{\sigma}^d(\mathbf{z}))$.

Combining approximations (a) and (b), the KL divergence in (28) can be written as

$$\mathcal{D}_{\text{kl}}(\pi^e(\mathbf{z} | \mathbf{b}) || \pi(\mathbf{z})) = \frac{1}{2} \left(-\log |\mathbf{D}^e(\mathbf{b})^2| - \ell + \boldsymbol{\mu}^e(\mathbf{b})^\top \boldsymbol{\mu}^e(\mathbf{b}) + \text{trace}\{\mathbf{D}^e(\mathbf{b})^2\} \right). \quad (31)$$

Then, with approximation (c), the ELBO simplifies to

$$\begin{aligned} \mathcal{L}(\boldsymbol{\theta}^e, \boldsymbol{\theta}^d) = \mathbb{E}_{\pi^e(\mathbf{z}|\mathbf{b})} & \left(-\frac{q}{2} \log(2\pi) - \log |\mathbf{D}^d(\mathbf{z})| - \frac{1}{2} \|\mathbf{D}^d(\mathbf{z})^{-1}(\mathbf{x} - \boldsymbol{\mu}^d(\mathbf{z}))\|_2^2 \right) \\ & - \frac{1}{2} \left(-\log |\mathbf{D}^e(\mathbf{b})^2| - \ell + \boldsymbol{\mu}^e(\mathbf{b})^\top \boldsymbol{\mu}^e(\mathbf{b}) + \text{trace}\{\mathbf{D}^e(\mathbf{b})^2\} \right). \end{aligned} \quad (32)$$

In the case where $\mathbf{D}^d(\mathbf{z}) \equiv \eta \mathbf{I}$, where $\eta > 0$ is a constant and \mathbf{I} is an identity matrix, the cost function (32) (sans constant) reduces to

$$\mathbb{E}_{\pi^e(\mathbf{z}|\mathbf{b})} \left(-\frac{1}{2\eta^2} \|\mathbf{x} - \boldsymbol{\mu}^d(\mathbf{z})\|_2^2 \right) - \frac{1}{2} \left(-\log |\mathbf{D}^e(\mathbf{b})^2| - \ell + \boldsymbol{\mu}^e(\mathbf{b})^\top \boldsymbol{\mu}^e(\mathbf{b}) + \text{trace}\{\mathbf{D}^e(\mathbf{b})^2\} \right). \quad (33)$$

A good guess for η can significantly reduce the complexity of minimizing the cost function.

Note that this is for one sample, so the overall goal is

$$\max_{\boldsymbol{\theta}^e, \boldsymbol{\theta}^d} \sum_{j=1}^J \mathcal{L}^j(\boldsymbol{\theta}^e, \boldsymbol{\theta}^d) \quad (34)$$

where $\mathcal{L}^j(\boldsymbol{\theta}^e, \boldsymbol{\theta}^d)$ is defined (32) for $(\mathbf{b}^j, \mathbf{x}^j)$. A standard optimization algorithm such as ADAM can be used to solve (34). See Algorithm 1 for a general outline.

Algorithm 1 Learning VED networks

- 1: **input** $\{(\mathbf{b}^j, \mathbf{x}^j)\}_{j=1}^J$, initialize encoder e with $\boldsymbol{\theta}^e$, initialize decoder d with $\boldsymbol{\theta}^d$
 - 2: **for** $k = 1, 2, \dots$ (optimization steps) **do**
 - 3: Get minibatch
 - 4: **for** j in the minibatch (loop over elements in minibatch) **do**
 - 5: Forward propagate encoder $[\boldsymbol{\mu}^e, \boldsymbol{\sigma}^e] = e(\mathbf{b}^j; \boldsymbol{\theta}^e)$
 - 6: Generate L samples from the latent space $\mathbf{z}^l \sim \mathcal{N}(\boldsymbol{\mu}^e, \text{diag}(\boldsymbol{\sigma}^e)^2)$
 - 7: **for** $l = 1, \dots, L$ (loop over samples from latent space) **do**
 - 8: Evaluate decoder $[\boldsymbol{\mu}^d, \boldsymbol{\sigma}^d] = d(\mathbf{z}^l; \boldsymbol{\theta}^d)$
 - 9: **end for**
 - 10: Compute loss \mathcal{L}^j and gradient $\nabla \mathcal{L}^j$
 - 11: **end for**
 - 12: Update $\boldsymbol{\theta}^e$ and $\boldsymbol{\theta}^d$
 - 13: **end for**
 - 14: **output** $\boldsymbol{\theta}^e$ and $\boldsymbol{\theta}^d$
-

3.2 Quantifying uncertainties in the QoI

In this section, we discuss how to estimate and perform UQ on QoI \mathbf{x} for a trained VED network, given an unobserved vector \mathbf{b} . In the context of goal-oriented inverse problems, a common approach to estimate the QoI is to use point estimates, e.g., the mean or the maximum of the posterior predictive. However, to quantify uncertainties for goal-oriented inverse problems one may need to compute the higher central moments of the posterior predictive, which in this case is computationally prohibitive. Hence, we first relate the outputs of the trained VED with the posterior predictive, describe how to sample from the posterior, and then utilize generated samples to estimate uncertainties for the QoI.

The following result relates the posterior-predictive with the output of the VED network. Let B, Z , and X denote random variables with corresponding probability densities $\pi(\mathbf{b}), \pi(\mathbf{z})$, and $\pi(\mathbf{x})$. The posterior predictive is related to the output of the VED according to

$$\pi_{\text{pred}}(\mathbf{x} | \mathbf{b}) = \mathbb{E}_{\mathbf{z}|\mathbf{b}} \pi(\mathbf{x} | \mathbf{z}, \mathbf{b}). \quad (35)$$

To see this, notice that

$$\pi_{\text{pred}}(\mathbf{x} | \mathbf{b}) = \int_{\mathbb{R}^\ell} \pi(\mathbf{x}, \mathbf{z} | \mathbf{b}) d\mathbf{z} = \int_{\mathbb{R}^\ell} \pi(\mathbf{x} | \mathbf{b}, \mathbf{z})\pi(\mathbf{z} | \mathbf{b}) d\mathbf{z} = \mathbb{E}_{\mathbf{z}|\mathbf{b}} \pi(\mathbf{x} | \mathbf{z}, \mathbf{b}). \quad (36)$$

Here, we used the definition of marginalization in the first equality and the conditional probability in the second equality. We refer to $\mathbb{E}_{\mathbf{z}|\mathbf{b}} \pi(\mathbf{x} | \mathbf{z}, \mathbf{b})$ as the *VED posterior predictive distribution*.

In the case where $\pi(\mathbf{b} | \mathbf{z}) = \pi(\mathbf{b} | \mathbf{x}, \mathbf{z})$, we can further simplify (36). Let us first reformulate the joint distribution $\pi(\mathbf{x}, \mathbf{z}, \mathbf{b})$.

$$\pi(\mathbf{x}, \mathbf{z}, \mathbf{b}) = \pi(\mathbf{b} | \mathbf{x}, \mathbf{z})\pi(\mathbf{x}, \mathbf{z}) = \pi(\mathbf{b} | \mathbf{z})\pi(\mathbf{x}, \mathbf{z}) = \frac{\pi(\mathbf{b}, \mathbf{z})}{\pi(\mathbf{z})}\pi(\mathbf{x}, \mathbf{z}) = \pi(\mathbf{b}, \mathbf{z})\pi(\mathbf{x} | \mathbf{z}). \quad (37)$$

Here, we used the additional assumption in the second equality. Now we have

$$\pi(\mathbf{x} | \mathbf{b}, \mathbf{z}) = \frac{\pi(\mathbf{x}, \mathbf{z}, \mathbf{b})}{\pi(\mathbf{z}, \mathbf{b})} = \frac{\pi(\mathbf{b}, \mathbf{z})\pi(\mathbf{x} | \mathbf{z})}{\pi(\mathbf{b}, \mathbf{z})} = \pi(\mathbf{x} | \mathbf{z}). \quad (38)$$

This simplifies (36) to

$$\pi_{\text{pred}}(\mathbf{x} | \mathbf{b}) = \mathbb{E}_{\mathbf{z}|\mathbf{b}} \pi(\mathbf{x} | \mathbf{z}). \quad (39)$$

Note that the expectation in the right-hand side of (35) is with respect to \mathbf{z} . Therefore, the VED-posterior is a probability distribution with respect to \mathbf{x} .

Now we discuss how to generate samples from the VED posterior-predictive and perform UQ, using the VED network. Suppose that an observation vector \mathbf{b} is provided. We then form the random variable $Z | B$. Note that this has a Gaussian distribution $\mathcal{N}(\boldsymbol{\mu}^e, \text{diag}(\boldsymbol{\sigma}^e)^2)$. We generate samples $\{\mathbf{z}^l\}_{l=1, \dots, L}$ from this distribution. For each of these samples from the latent space, we evaluate the decoder $d(\mathbf{z}^l; \boldsymbol{\theta}^d)$, and sample from the Gaussian distribution $\mathcal{N}(\boldsymbol{\mu}^d, \text{diag}(\boldsymbol{\sigma}^d)^2)$. The target has $N_{\text{sample}} = L \cdot K$ samples from the VED posterior predictive.

Note that we can estimate the mean of the VED-posterior $\boldsymbol{\mu}_{\text{VED}}$ using

$$\boldsymbol{\mu}_{\text{VED}} = \mathbb{E}_{\mathbf{x}} \mathbb{E}_{\mathbf{z}|\mathbf{b}} \pi(\mathbf{x} | \mathbf{z}, \mathbf{b}) \approx \frac{1}{L} \sum_{i \leq L} \mathbb{E}_{\mathbf{z}^i|\mathbf{b}} \pi(\mathbf{x} | \mathbf{z}^i, \mathbf{b}) = \frac{1}{L} \sum_{l \leq L} \boldsymbol{\mu}^d(\mathbf{z}^l). \quad (40)$$

4 Numerical Results

In this section, we consider two examples from inverse problems, where the aim is to perform UQ for some quantities of interest. The QoI is different in each example. In Section 4.1, the goal is to perform UQ on the regularization parameter required to compute tomography reconstructions using total variation

Algorithm 2 Sampling for go-UQ

- 1: **input** \mathbf{b} , encoder e that depends on parameters θ^e , decoder d that depends on parameters θ^d
 - 2: Evaluate encoder $[\boldsymbol{\mu}^e, \boldsymbol{\sigma}^e] = e(\mathbf{b}; \theta^e)$
 - 3: Generate L samples from the latent space $\mathbf{z}^l \sim \mathcal{N}(\boldsymbol{\mu}^e, \text{diag}(\boldsymbol{\sigma}^e)^2)$
 - 4: **for** $l = 1, 2, \dots, L$ **do**
 - 5: Evaluate decoder $[\boldsymbol{\mu}^d, \boldsymbol{\sigma}^d] = d(\mathbf{z}^l; \theta^d)$
 - 6: Generate κ samples $\mathbf{x}_k^l \sim \mathcal{N}(\boldsymbol{\mu}^d, \text{diag}(\boldsymbol{\sigma}^d)^2)$
 - 7: **end for**
 - 8: **output** $\{\mathbf{x}_k^l\}_{k=1, \dots, \kappa; l=1, \dots, L}$ samples from VED predictive posterior
-

regularization. In Section 4.2, we consider a hydraulic tomography example, where the QoI represents expansion coefficients defining a piecewise constant conductivity field. In both instances, we sample from the predictive posterior and bypass the intermediate reconstructions (i.e., the tomography reconstruction and the conductivity field reconstruction, respectively).

4.1 Experiment 1: X-ray Computed Tomography (CT)

X-ray CT is an imaging technique that uses a combination of X-ray exposure and computational procedures to construct cross-sectional images of an object. When an object is exposed to an X-ray, its material attenuates the radiation whereas the amount of attenuation depends on the material’s properties. The interaction between the object and the X-ray can be modeled as a line integral and is referred to as the Beer–Lambert law [25]. The transformation that takes an object (an attenuation field) into its line integrals is mathematically modeled as a linear transformation and is referred to as the *Radon transform* [25]. The transformed function is referred to as a *sinogram*. The CT reconstruction aims to infer the attenuation field from its Radon transform, however, this inversion process is ill-posed, and stabilization through regularization is required.

Let $\mathbf{y} \in \mathbb{R}^n$ be a vectorized 2-dimensional discretized and unknown attenuation field and let $\mathbf{b} \in \mathbb{R}^m$ be the noisy sinogram. Consider the model given in (1), where $F(\mathbf{y})$ denotes the discrete Radon transform of \mathbf{y} . The corresponding variational inverse problem can be written as a deterministic minimization problem

$$\mathbf{y}(x) = \arg \min_{\mathbf{y}} \|F(\mathbf{y}) - \mathbf{b}\|_2^2 + x \|\mathbf{D}\mathbf{y}\|_1, \quad (41)$$

where the first term represents the data fidelity and the second term is the regularization term. Here we promote piecewise constant solutions in \mathbf{y} by utilizing a 1-norm and a first-order two-dimensional finite difference operator \mathbf{D} , [26, 45], representing a total variation regularizer. The balance between the two terms in this minimization problem is established by the regularization parameter $x > 0$.

The regularization parameter is a priori unknown and choosing an appropriate x can be a challenging task [15, 16, 21, 39, 51]. Suppose that a true attenuation field \mathbf{y}_{true} is available, then one way to select x is to solve a bilevel optimization problem

$$\hat{x} = \arg \min_x \|\mathbf{y}(x) - \mathbf{y}_{\text{true}}\|_2^2, \quad \text{where } \mathbf{y}(x) \text{ is given in (41)}. \quad (42)$$

The optimization problem in (41) is regarded as the inner minimization problem with a fixed regularization parameter x . The minimization problem in (42) is referred to as the *design problem* which seeks the optimal regularization parameter. A bilevel optimization problem of type (42) is, in general, non-convex. The alternating direction method of multipliers (ADMM) method can be used to solve the inner-minimization problem and a Bayesian optimization method can be used to solve the outer-minimization problem [7]. In [1], it was shown that DNNs can be trained to represent the mapping $\mathbf{b} \mapsto \hat{x}$, but the framework did not allow for UQ. Furthermore, it was observed that uncertainties in \hat{x} arise due to challenges in optimization in (42) and numerical evaluation of its solution. Thus, it is possible that a numerical solution for (42) is far from the optimal regularization parameter.

Description of training In this work, we train a VED network to represent the mapping $\mathbf{b} \mapsto \hat{x}$. Hence, in addition to obtaining a VED-predicted regularization parameter, we can efficiently draw samples from the VED predictive posterior and these samples allow us to quantify the uncertainty in the predicted parameter. In this context, given \mathbf{y}_{true} , the prediction operator G corresponds to solving the bi-level minimization (42) to find the optimal regularization parameter, i.e., $\hat{x} = G(\mathbf{y}_{\text{true}})$ is a numerically evaluated optimal regularization parameter. For the training data, we generate $J = 24,000$ images $\mathbf{y}_{\text{true}}^j, j = 1, \dots, J$ as randomized Shepp-Logan phantoms [8, 46]. Then the training data are given by, $\left\{ F(\mathbf{y}_{\text{true}}^j) + \mathbf{e}^j, G(\mathbf{y}_{\text{true}}^j) \right\}_{j=1}^J$. For simplicity, we assume $F(\mathbf{y}) = \mathbf{A}\mathbf{y}$, where \mathbf{A} is a matrix representing parallel beam tomography (with 181 parallel rays over 180 equidistant angles). The noisy sinogram is then given by

$$\mathbf{b}^j = \mathbf{A}\mathbf{y}_{\text{true}}^j + \mathbf{e}^j. \quad (43)$$

The noise vector \mathbf{e}^j in (43) is chosen to be white noise with a varying noise level that is selected uniformly random between 0.1% and 5%. A noise level of $r\%$ corresponds to a noise vector \mathbf{e}^j satisfying $\|\mathbf{e}^j\|_2 / \|\mathbf{A}\mathbf{y}_{\text{true}}^j\|_2 = r/100$.

The architecture of the VED network is illustrated in Figure 5. The encoder network is comprised of convolutional layers and ReLU layers [20]. The dimension of the latent space is set to $\ell = 128$. The decoder network is a feed-forward fully-connected ReLU network with one hidden layer. This architecture is chosen to exploit local correlations in the intensities in a sinogram, but other architectures can be considered. We observe that other network architectures result in similar results (data not shown). The VED is trained by minimizing the cost function (33), with $\eta = 0.1$ using the ADAM optimization method [28]. The optimization process is stopped after 10^4 epochs. The learning rate is adjusted dynamically from the interval $[5 \cdot 10^{-2}, 10^{-4}]$.

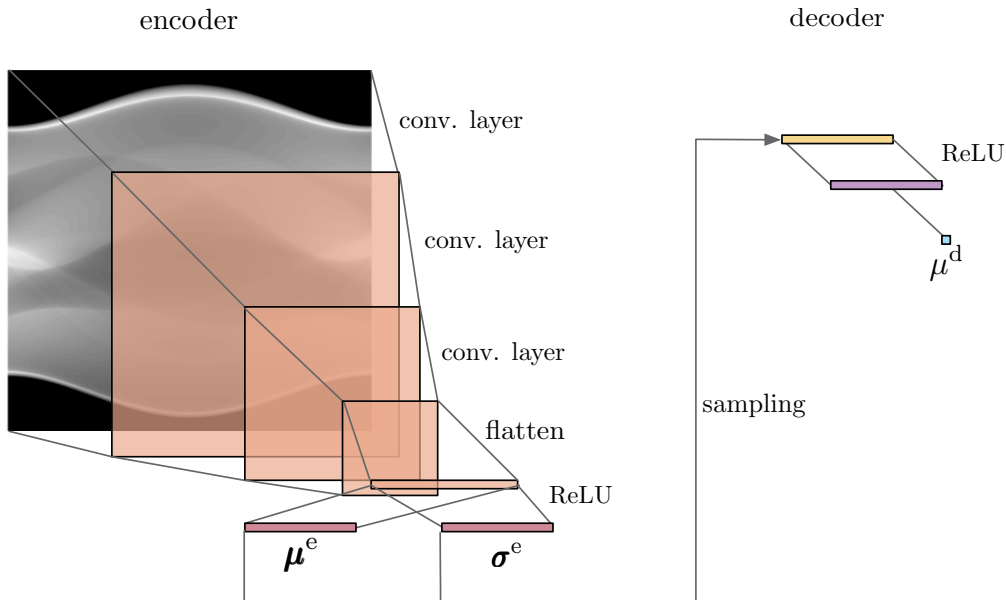


Figure 5: Architecture of the VED network for the X-ray CT problem, where the goal is to perform UQ on the regularization parameter. On the left is the encoder network that maps the input sinogram to the latent space (defined by mean μ^e and standard deviations σ^e). On the right is the decoder network that maps samples from the latent distribution to the output regularization parameter (defined by mean μ^d).

Evaluation of VED To test the performance and generalizability of the learned VED network, we consider three datasets outside the training dataset. First, we consider an example from the test data. We generate

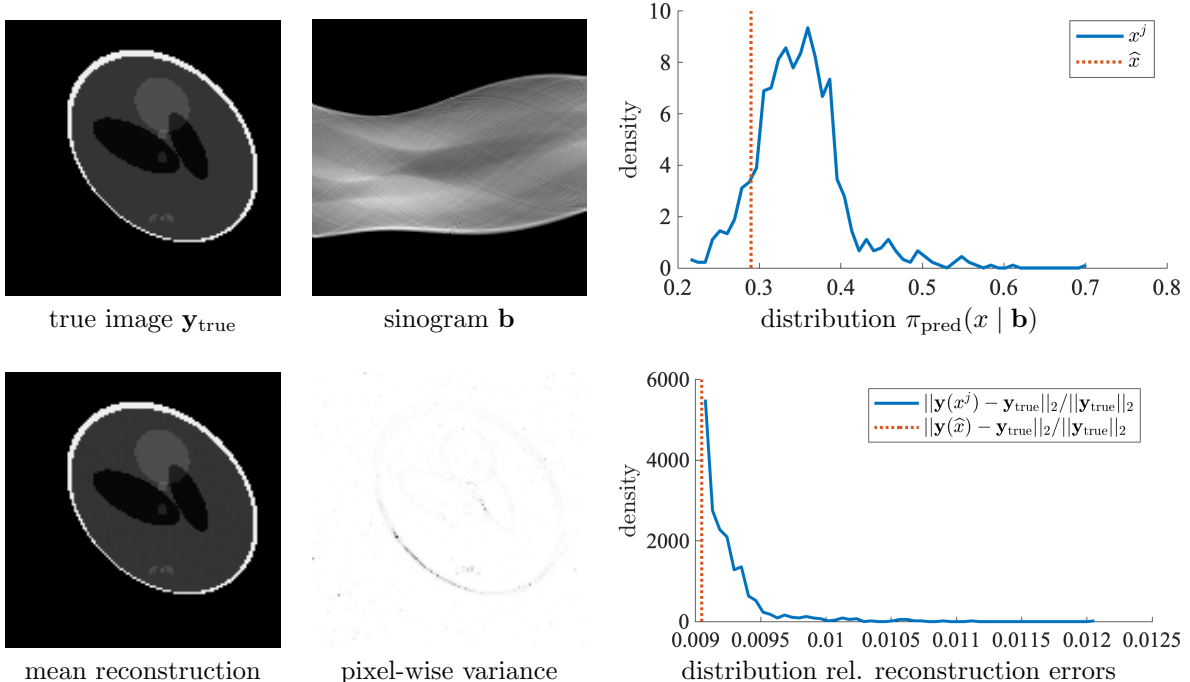


Figure 6: The trained VED network from the X-ray CT experiment is used to perform UQ on the regularization parameter for a test data sample. In the top row, we provide the true image, the corresponding noisy sinogram, and the distribution of the predicted regularization parameters x^j from $\pi_{\text{pred}}(x | \mathbf{b})$ with the QoI \hat{x} provided for reference. In the bottom row, we provide the mean reconstruction, the image of pixel-wise uncertainties (in inverted colormap so that large variances are denoted in black), and the distribution of the relative reconstruction errors.

a sinogram from a randomized Shepp-Logan phantom and add noise. The true image and sinogram are provided in the top row of Figure 6. Using the approach described in Section 3.2, we generate 10^3 samples x^j from the VED predictive posterior. The distribution of these samples is provided in the top row of Figure 6. Notice that the VED predicted values for the regularization parameter are within the interval $[0.2, .7]$, with a high probability of being close to the optimal regularization parameter $\hat{x} = G(\mathbf{y}_{\text{true}})$. To visualize the corresponding uncertainties in the reconstructed images, for each of the samples of the regularization parameter, we solve (41) to get a reconstruction $\mathbf{y}(x^j)$. The mean reconstruction image, an image of the pixel-wise variances (in inverted colormap so that white corresponds to small variances and black corresponds to larger variances), and the distribution of relative reconstruction errors are provided in the bottom row of Figure 6. Similar to observations made in [2, 50], we observe that large uncertainties occur at the locations of discontinuities in the image. Furthermore, as expected, the relative reconstruction errors for samples from the posterior predictive are larger than the relative reconstruction error corresponding to the optimal regularization parameter (denoted by the red dotted vertical line), but the distribution of relative reconstruction errors is tight, implying a high probability of a good reconstruction.

For the second out-of-sample dataset, we generate a sinogram from a randomized Shepp-Logan phantom, but we modify the projection angles. That is, we use a forward model matrix \mathbf{A} where the 180 projections angles are no longer equidistant. We add white noise to the vector of projection angles with a standard deviation of 0.1. The sinogram is propagated through the trained VED network, and we draw 10^3 samples of the regularization parameter from the VED-posterior predictive $\pi_{\text{pred}}(x | \mathbf{b})$. The true image, the sinogram corresponding to modified angles, and the distribution of the regularization parameter samples are provided

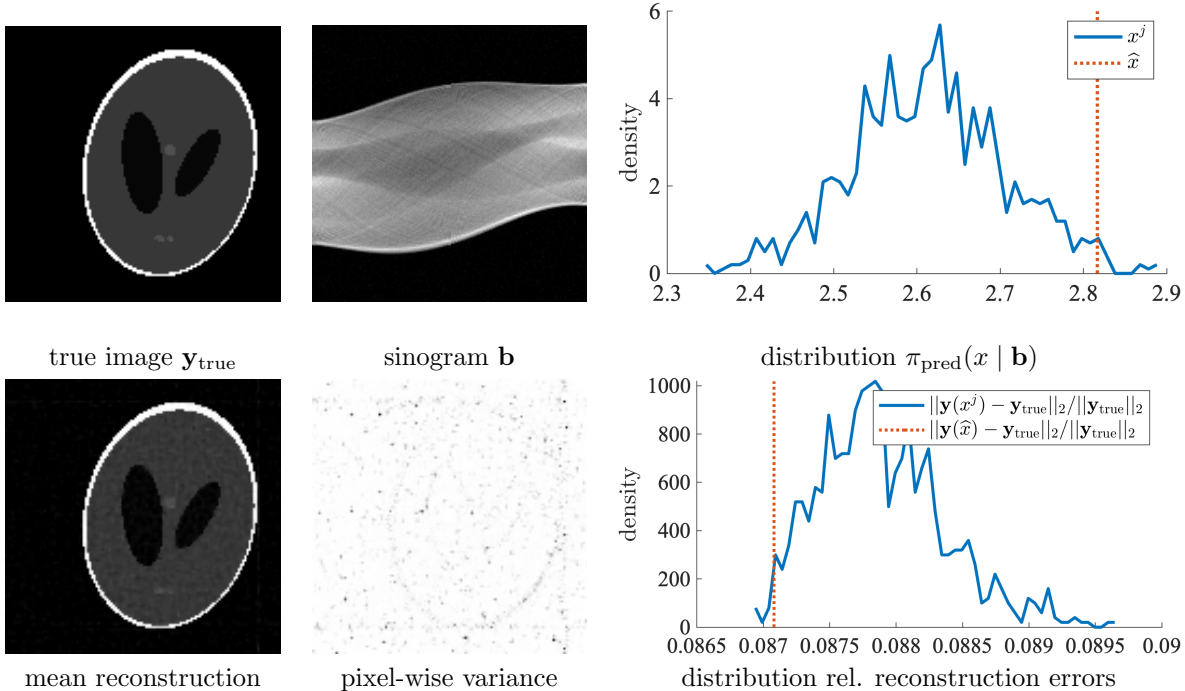


Figure 7: UQ on the regularization parameter via a trained VED network for x-ray CT reconstruction with modified angles.

in the top row of Figure 7. Although the QoI \hat{x} is slightly larger than many of the predicted values, the range is fairly small. The mean reconstruction, pixel-wise variances for the reconstruction, and the distribution of relative reconstruction errors are provided in the bottom row of Figure 7. Obtaining relative errors smaller than the optimal can be attributed to numerical errors in solving (42).

For the third out-of-sample experiment, we use data for the tomographic reconstruction of a walnut given at [22]. The walnut image, which was computed using a CT scan but that we take as ground truth, is provided in the top row of Figure 8 along with a noisy sinogram that was generated as in (43). Similar to the previous experiment, we draw 10^3 samples of the regularization parameter from the VED-posterior predictive $\pi_{\text{pred}}(x | \mathbf{b})$. For this example, we observe that the trained VED network provides a wide range of values for the predicted regularization parameter, but all of the samples are not too far from the QoI \hat{x} . The mean reconstruction and pixel-wise variances are provided in the bottom row of Figure 8, along with the distribution of relative reconstruction errors. Again, we see that large uncertainties are present at the locations of the discontinuities in the image, and the relative reconstruction error norms for the sampled regularization parameters are close to that of the optimal regularization parameter for this problem.

4.2 Experiment 2: Nonlinear Hydraulic Tomography

Next, we consider an example where the goal is to detect the locations of discontinuities in reconstructed images. A typical approach (e.g., used in CT) is to obtain an image reconstruction using standard algorithms, followed by post-processing, e.g., with image segmentation. We consider an approach that avoids the intermediate step and goes directly from the observation to the discontinuities [2, 11]. Although the QoI could represent locations of the discontinuities, instead we consider a nonlinear hydraulic tomography problem that is adopted from [6, 32, 44] and define the QoI to be coefficients representing a parameterization of the locations of the discontinuities. Then, we use VEDs to obtain uncertainties for the coefficients.

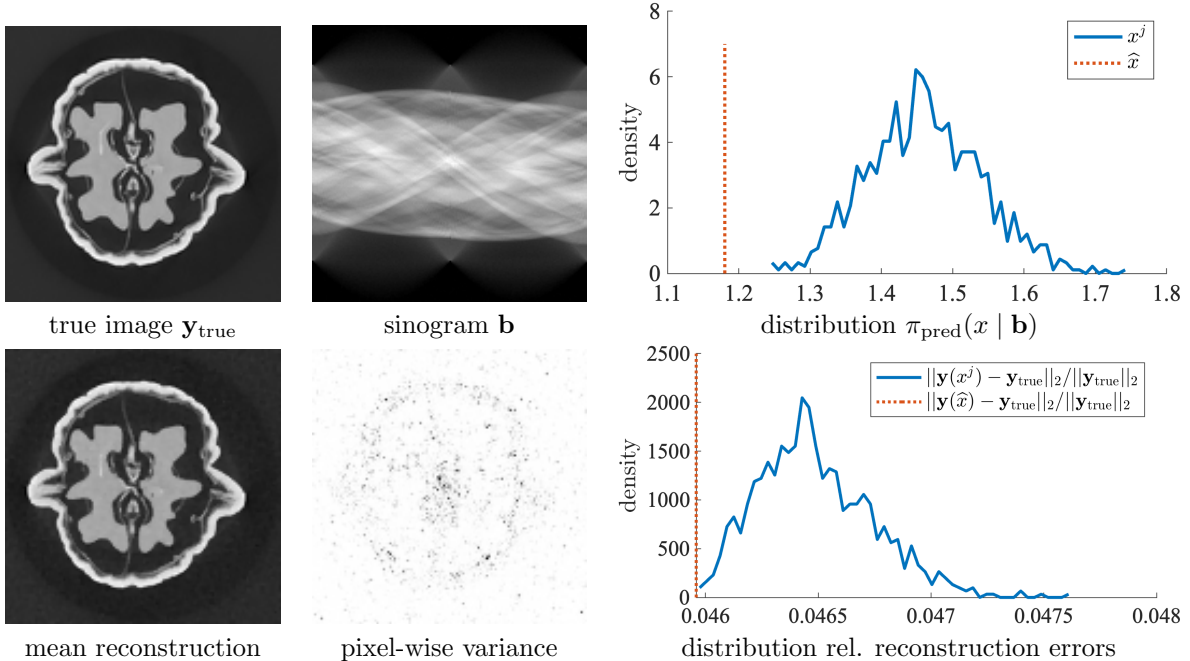


Figure 8: UQ on the regularization parameter via a trained VED network for an out-of-sample walnut image, [22].

Consider a confined aquifer that is modeled using an elliptic partial differential equation (PDE),

$$\nabla \cdot (y(\boldsymbol{\xi}) \nabla u(\boldsymbol{\xi})) = q_i \delta(\boldsymbol{\xi}_i^{\text{well}}), \quad \boldsymbol{\xi} = (\xi_1, \xi_2) \in \mathcal{D}, \quad (44)$$

where $\mathcal{D} \subset \mathbb{R}^2$ is the unit square domain, $u : \mathbb{R}^2 \rightarrow \mathbb{R}$ is the hydraulic head, $y : \mathbb{R}^2 \rightarrow \mathbb{R}^+$ is the hydraulic conductivity, $\{\boldsymbol{\xi}_i^{\text{well}}\}_{i=1}^{N_{\text{well}}}$ are locations for N_{well} wells, and q_i is the pumping rate at the i -th well. We consider a zero-head (homogeneous Dirichlet) boundary condition on the left, right, and bottom boundaries of \mathcal{D} . Furthermore, we consider a no-flux (homogeneous Neumann) boundary condition on the top boundary. We discretize and solve (44) using a finite element method (FEM) on a structured mesh with $N_{\text{FEM}} = 10,201$ degrees of freedom (on a grid of approximate size 100×100).

We begin by describing the forward process. Assume we have the domain \mathcal{D} and the true hydraulic conductivity provided in Figure 10a. Consider placing 20 wells in the domain \mathcal{D} located at coordinates $(i/4, j/5)$, with integers $1 \leq i \leq 4$ and $1 \leq j \leq 5$. At the i -th well, we perform an injection at the rate of q_i . We measure the head at the rest of the $(N_{\text{well}} - 1)$ wells and repeat the injection for all wells. Thus, our measurement vector \mathbf{b} is of size $N_{\text{well}}(N_{\text{well}} - 1)$, where the k -th component of \mathbf{b} is given as

$$b_k = u_y^i(\boldsymbol{\xi}_j) + e_k, \quad k = i \cdot N_{\text{well}} + j, \text{ and, } i \neq j, \quad (45)$$

where u_y^i is the solution to (44) when the conductivity is y and the injection is at the i -th well, and e_k represents error in the observation. Note that the parameter to observation map F in (1) corresponds to the map $y \mapsto \mathbf{b}$. We consider a noise level of 1%, i.e., \mathbf{e} containing errors e_k is a realization of a mean-zero Gaussian multivariate random variable with covariance matrix $\sigma_n^2 \mathbf{I}$ where

$$\sigma_n = \frac{\sqrt{\sum_{i=1}^{N_{\text{well}}} (u_y^i)^2}}{100}. \quad (46)$$

Given measurements \mathbf{b} , the aim of the hydraulic tomography inverse problem is to reconstruct the hydraulic conductivity.

We define a goal-oriented prior distribution for $y(\boldsymbol{\xi})$. Let V be a zero-mean multivariate Gaussian random vector of size N_{FEM} , distributed according to the covariance operator $\mathcal{C} = (\epsilon_{\text{cl}}^2 \mathbf{I} + \Delta)^{-1}$, with $\epsilon_{\text{cl}} = 1/0.1$, and, \mathbf{I} and \mathbf{L} , the identity and the Laplacian operators, respectively. We now construct a piece-wise constant conductivity field

$$y(\boldsymbol{\xi}) = a^+ H(V(\boldsymbol{\xi})) + a^- (1 - H(V(\boldsymbol{\xi}))), \quad (47)$$

where H is the Heaviside step function, and, $a^+, a^- > 0$ are positive constants. Note that we can approximate V using the eigendecomposition of \mathcal{C} as

$$V(\boldsymbol{\xi}) \approx \sum_i^{N_{\text{goal}}} X_i \sqrt{g_i} v_i(\boldsymbol{\xi}), \quad (48)$$

where $\{(g_i, v_i(\boldsymbol{\xi}))\}_{i \leq N_{\text{goal}}}$ are the eigenpairs of \mathcal{C} associated with the largest eigenvalues of \mathcal{C} sorted in decreasing order. Furthermore, X_i 's are independent and standard normal random variables. We define the goal of the inverse problem to be the coefficients X_i in (48). Let $N_{\text{goal}} = 32$, then the QoI are parameters $\mathbf{x} \in \mathbb{R}^{32}$, and the prediction operator G , in (1) corresponds to the map $y \mapsto \mathbf{x}$.

Description of training We collect a dataset of pairs $\{(\mathbf{b}^j, \mathbf{x}^j)\}_{j=1}^J$, with $J = 10^4$ where \mathbf{x}^j are realizations from the standard normal distribution, and \mathbf{b}^j has components described in (45). We then consider the VED network summarized in Figure 9 for the hydraulic tomography problem. Note that in this example, we do not know the mean and the standard deviations of the target. We consider a Gaussian multi-layer perceptron output layer that estimates these values with 2 output layers. The cost function for this network can be constructed following (32), and the network is trained using the ADAM optimization algorithm [28] over 1.5×10^4 epochs. The learning rate is dynamically adjusted from $[5 \times 10^{-2}, 10^{-4}]$.

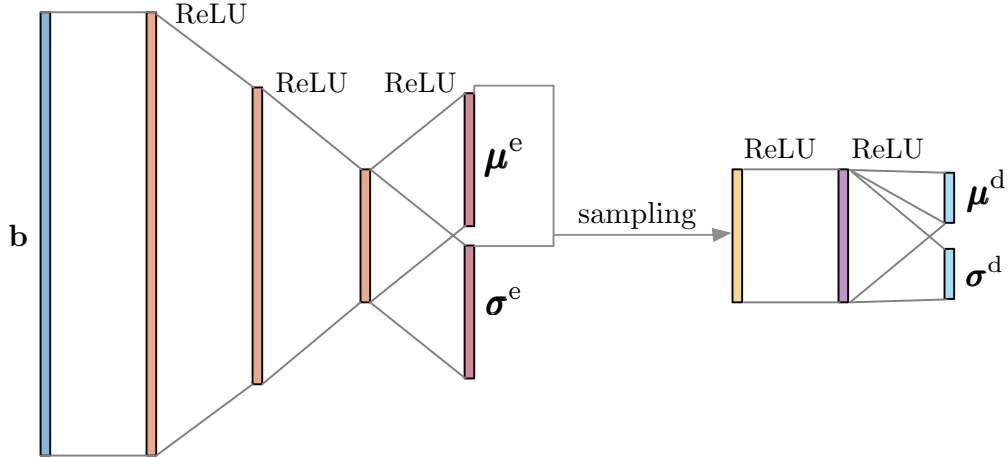


Figure 9: Architecture of the VED network for the hydraulic tomography problem, where the goal is to perform UQ on the parameters describing the discontinuities in the conductivity. On the left is the encoder network that maps the input, hydraulic head at the location of the wells, to the latent space (defined by mean $\boldsymbol{\mu}^e$ and standard deviations $\boldsymbol{\sigma}^e$). On the right is the decoder network that maps samples from the latent distribution to the target discontinuity parameters (defined by mean $\boldsymbol{\mu}^d$ and standard deviations $\boldsymbol{\sigma}^d$).

Evaluation of VED We evaluate the performance of the trained VED network for an out-of-sample test problem of finding the hydraulic conductivity field in Figure 10a, which is constructed by placing disks centered at coordinates $(0.3, 0.65)$ and $(0.25, 0.65)$ with radii 0.15 and 0.25 and conductivity values set to $a^+ = 10$ and $a^- = 1$, inside and outside of the disk inclusions, respectively. Note that this conductivity

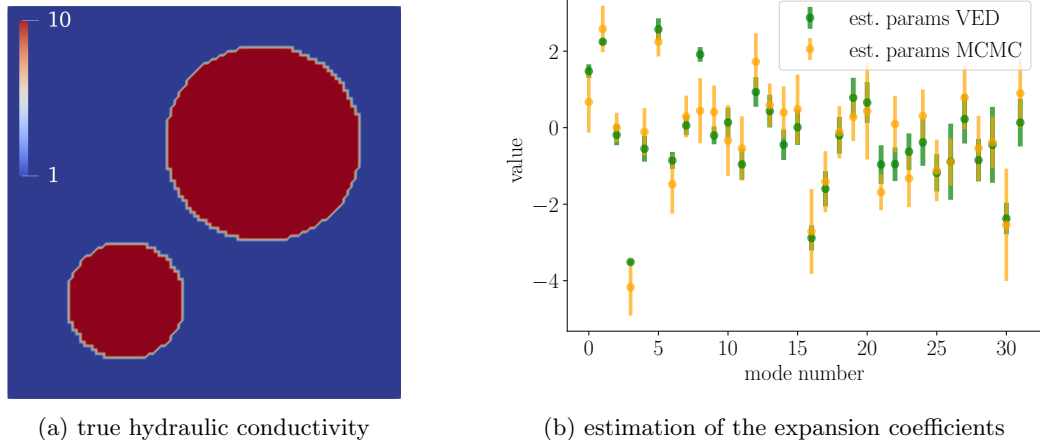


Figure 10: Results for the nonlinear hydraulic tomography example. In (a), we provide the true hydraulic conductivity field. In (b), we provide the estimated expansion coefficients and associated 99% credibility intervals (indicated by bars) using samples from the VED posterior predictive and using MCMC samples. The mode number corresponds to the index i for coefficient X_i .

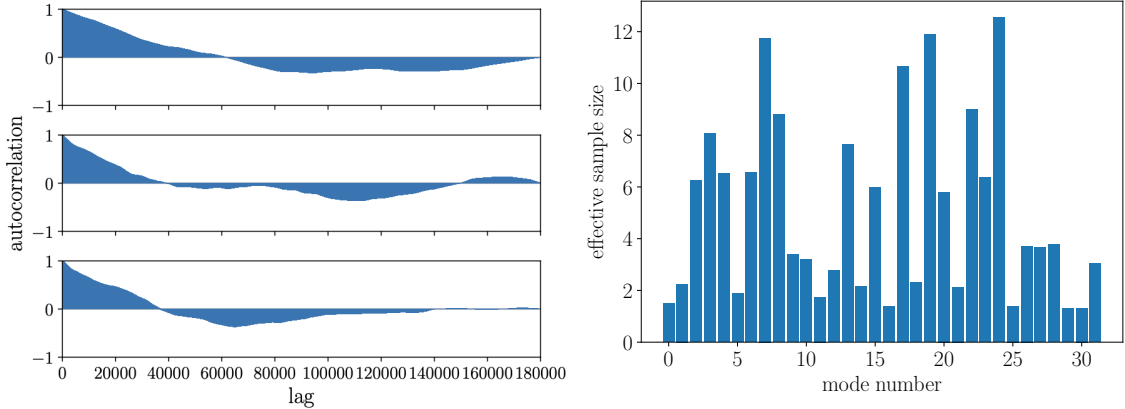
field does not belong to the training dataset and is not generated from the prior distribution (48) and (47). A measurement vector \mathbf{b} is generated as in (45), and we follow Algorithm 2 to draw samples from the VED posterior predictive distribution. In Figure 10b, we provide the mean of the posterior-predictive, i.e., the 32 expansion coefficients in \mathbf{x} using the VED (in green) along with the 99% credibility intervals. For comparison purposes, we use a Markov Chain Monte Carlo (MCMC) method to obtain a sequence of samples $\{\mathbf{x}_{\text{MCMC}}^j\}_{j=1}^{N_{\text{MCMC}}}$, from the posterior-predictive. MCMC methods allow for estimation of moments, e.g., $\mathbb{E}(f(X))$ can be estimated using the ergotic sum

$$\mathbb{E}(f(X)) \approx \frac{1}{N_{\text{MCMC}}} \sum_{j=1}^{N_{\text{MCMC}}} f(\mathbf{x}_{\text{MCMC}}^j). \quad (49)$$

We estimate the mean of the posterior-predictive $\mathbb{E}(X)$ by taking f to be the identity map in (49). Similarly, we estimate the variance by taking $f(X) = (X - \mathbb{E}(X))^2$. The preconditioned Crank-Nicolson (pCN) method [9] was used for this problem because of its suitability for expansions of the form (48) [9]. We provide means and variances of the estimated expansion coefficients (in yellow) in Figure 10b. We notice a correlation between the two methods, suggesting that the mean of the VED-posterior predictive correctly approximates the mean of the actual posterior predictive.

The convergence of the sum in (49) for a general posterior distribution is an ongoing topic of research. One indication for convergence is the effective sample size (ESS) [40] of MCMC samples, which suggests how many of the MCMC samples can be regarded as independent samples. Larger ESS values indicate a better approximation in (49). In this example, we compute 2×10^5 samples from the posterior predictive using the pCN sampler and discard the first 50×10^4 samples as the burn-in period. Figure 11a shows the autocorrelation function [40] of the samples for the first 3 expansion coefficients in (48). We observe a similar behavior for the other coefficients. We notice that it takes about 50×10^4 samples for the autocorrelation function to reach zero. This suggests that the convergence of the MCMC is only achieved with a very large number of samples. In Figure 11b, we provide the ESS for each expansion coefficient. A reliable estimate of the variance of the posterior requires an ESS of around 100, so the ESS estimates in Figure 11b suggest that the estimated moments of the posterior cannot be trusted, even with 2×10^5 samples computed for this test case.

The bars in Figure 10b indicate 3 times the length of the standard deviation. The standard deviation is estimated from the samples of the posterior, in both methods. We emphasize that the MCMC estimates of



(a) auto-correlation function of the first 3 coefficients. (b) effective sample size for each expansion coefficient

Figure 11: For MCMC samples from the posterior predictive, we provide the autocorrelation function for the first three expansion coefficients in (a) and the effective sample size for each coefficient in (b).

the standard deviation cannot be trusted due to the low ESS. Regarding the VED estimates of the standard deviation, we see that the confidence in the estimates reduces for higher modes, i.e., larger indices. This behavior is also reported in other works, e.g. see [14, 44]. In addition, since samples provided by the VED posterior predictive are independent samples, the estimated variance can be trusted, up to the accuracy of the VED approximation.

Next, we provide some samples for visualization. In the first row of Figure 12, we provide samples from the prior distribution that were obtained by mapping random samples of the parameter vector \mathbf{x}^j onto the conductivity field \mathbf{y}^j following (48) and then (47). Then in the second and third rows of Figure 12, we provide conductivity fields corresponding to samples from the VED posterior predictive distribution and MCMC samples from the posterior predictive distribution, respectively. In terms of the conductivity field, we observe comparable samples.

To visualize the uncertainty in the QoI, one approach is to compute the variance of the posterior-predictive for each expansion coefficient X_i in (48) (see Figure 10b). Another approach is to compute the hydraulic conductivity for all samples from the posterior predictive distribution using the transformation (47), and then estimate means and variances in the conductivity space. These results are provided in Figure 13. Both methods correctly identify the two inclusions in the domain. The variance in both methods indicates a point-wise level of uncertainty in the estimation. Both methods show high certainty away from the boundaries of the inclusion and low certainty at the location of the boundaries. In addition, we see uncertainty at the boundary of the domain with the Newman boundary condition. However, as discussed above we cannot trust the uncertainty estimates for the MCMC method.

Finally, we compare the computational efficiency of the two methods by providing CPU times for computing 1000 samples and 10 independent samples from the posterior predictive in Table 1. All experiments were carried out on a MacBook Pro with an Apple M1 Pro processor. We notice that the ability to draw independent samples from the posterior-predictive provides significant computational gains. Recall that the number of samples required to train the neural network is 10^4 . This is orders of magnitude smaller than the number of samples required from the MCMC method to construct a representative set of independent samples from the posterior predictive distribution.

5 Conclusions

In this work, we describe VED networks for the direct estimation of QoI and their uncertainties for inverse problems, given observations. Following a supervised learning approach, we use training data to learn

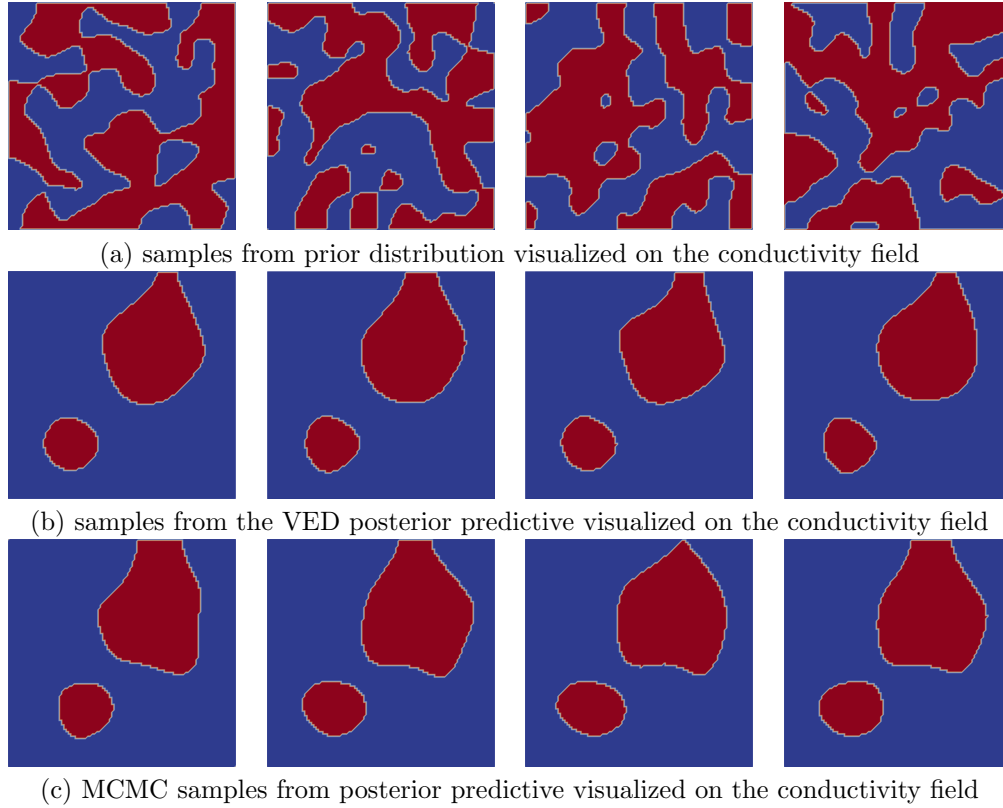


Figure 12: (a) Samples from the prior that were obtained by (48) and then (47) for random samples of the parameter vector \mathbf{x} . (b) Samples from the VED posterior predictive distribution mapped onto the conductivity field. (c) MCMC samples from the posterior predictive distribution mapped onto the conductivity field.

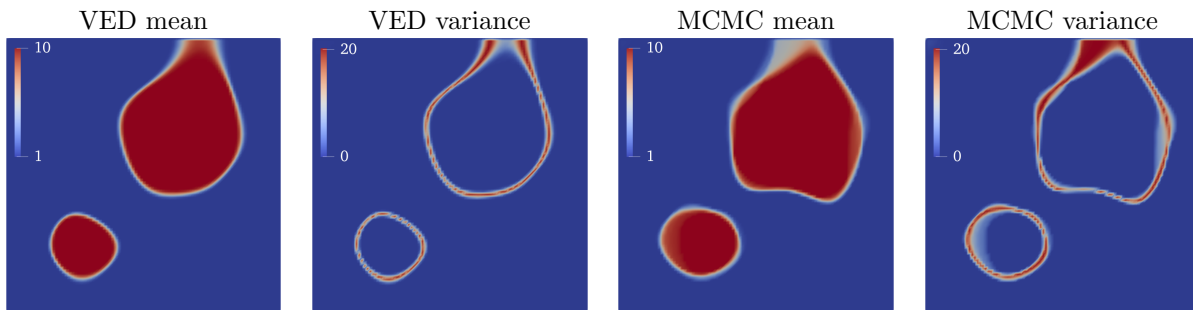


Figure 13: Means and variances of the conductivity fields for samples from the VED posterior predictive (left) and MCMC samples from the posterior predictive (right).

	Elapsed time (s) for computing 1000 samples	Elapsed time (s) for computing 10 <i>independent</i> samples
MCMC (pCN)	270	2.5×10^5
VED sampling	20	0.02
speed-up	13.5	1.2×10^8

Table 1: CPU times for sampling from the posterior predictive using MCMC versus using VED sampling. The speed-up in terms of obtaining independent samples is significant.

parameters defining a VED network, where an encoder maps an observation to a distribution over the latent space and a decoder maps samples from the latent space to distributions over the QoI output space. By leveraging probability distributions in both the latent space and in the posterior predictive, VED networks can be used to efficiently generate independent samples from the posterior predictive, thereby enabling efficient UQ for the QoI without requiring the use of expensive MCMC methods. The potential benefits of our approach for goal-oriented UQ are demonstrated by the numerical experiments for two scenarios. In Section 4.1, we demonstrate the use of VED networks for UQ of the regularization parameter for total variation for X-ray CT reconstruction, and in Section 4.2, we demonstrate the ability of trained VEDs to not only estimate locations but also uncertainties of discontinuities in nonlinear hydraulic tomography reconstructions.

Acknowledgement

This work was partially supported by the National Science Foundation (NSF) under grants DMS-1654175 and 2026841 (J. Chung), DMS-2152661 (M. Chung) and partially supported by The Villum Foundation Grant No. 25893 (B M Afkham)

We would like to express our sincere gratitude to Dr. Heydar M. Afkham for his invaluable contribution in designing the architecture of neural networks, which has greatly enhanced the accuracy and efficiency of the models in this paper.

References

- [1] B. M. Afkham, J. Chung, and M. Chung. “Learning regularization parameters of inverse problems via deep neural networks”. In: *Inverse Problems* 37.10 (2021), page 105017 (cited on pages 2, 5, 12).
- [2] B. M. Afkham, Y. Dong, and P. C. Hansen. “Uncertainty quantification of inclusion boundaries in the context of X-ray tomography”. In: *SIAM/ASA Journal on Uncertainty Quantification* 11.1 (2023), pages 31–61 (cited on pages 2, 14, 15).
- [3] A. Attia, A. Alexanderian, and A. K. Saibaba. “Goal-oriented optimal design of experiments for large-scale Bayesian linear inverse problems”. In: *Inverse Problems* 34.9 (2018), page 095009 (cited on pages 2, 4).
- [4] A. Bora et al. “Compressed sensing using generative models”. In: *International Conference on Machine Learning*. PMLR, 2017, pages 537–546 (cited on page 7).
- [5] D. Calvetti and E. Somersalo. *An Introduction to Bayesian Scientific Computing: Ten Lectures on Subjective Computing*. Volume 2. Springer Science & Business Media, 2007 (cited on page 3).
- [6] M. Cardiff and P. Kitanidis. “Bayesian inversion for facies detection: An extensible level set framework”. In: *Water Resources Research* 45.10 (2009) (cited on page 15).

- [7] J. Chung et al. “Efficient learning methods for large-scale optimal inversion design”. In: *Numerical Algebra, Control and Optimization* (2022). ISSN: 2155-3289. DOI: 10.3934/naco.2022036. URL: /article/id/63930a2980e8bc15ce45a91f (cited on page 12).
- [8] M. Chung. *Random-Shepp-Logan-Phantom*. 2020. URL: <https://github.com/matthiaschung/Random-Shepp-Logan-Phantom> (visited on 12/14/2020) (cited on page 13).
- [9] S. L. Cotter et al. “MCMC Methods for Functions: Modifying Old Algorithms to Make Them Faster”. In: *Statistical Science* 28.3 (2013), pages 424–446. DOI: 10.1214/13-STS421. URL: <https://doi.org/10.1214/13-STS421> (cited on page 18).
- [10] K. Cranmer, J. Brehmer, and G. Louppe. “The frontier of simulation-based inference”. In: *Proceedings of the National Academy of Sciences* 117.48 (2020), pages 30055–30062 (cited on page 7).
- [11] V. A. Dahl, A. B. Dahl, and P. C. Hansen. “Computing segmentations directly from x-ray projection data via parametric deformable curves”. In: *Measurement Science and Technology* 29.1 (2017), page 014003 (cited on pages 2, 15).
- [12] E. De Vito, M. Fornasier, and V. Naumova. “A machine learning approach to optimal Tikhonov regularization I: affine manifolds”. In: *Analysis and Applications* 20.02 (2022), pages 353–400 (cited on page 5).
- [13] R. DeVore et al. “Computing a quantity of interest from observational data”. In: *Constructive Approximation* 49.3 (2019), pages 461–508 (cited on page 2).
- [14] M. M. Dunlop and A. M. Stuart. “The Bayesian formulation of EIT: Analysis and algorithms”. In: *Inverse Problems & Imaging* 10.4 (2016), page 1007 (cited on page 19).
- [15] C. G. Farquharson and D. W. Oldenburg. “A comparison of automatic techniques for estimating the regularization parameter in non-linear inverse problems”. In: *Geophysical Journal International* 156.3 (2004), pages 411–425 (cited on page 12).
- [16] N. P. Galatsanos and A. K. Katsaggelos. “Methods for choosing the regularization parameter and estimating the noise variance in image restoration and their relation”. In: *IEEE Transactions on Image Processing* 1.3 (1992), pages 322–336 (cited on page 12).
- [17] M. Glöckler, M. Deistler, and J. H. Macke. “Variational methods for simulation-based inference”. In: *International Conference on Learning Representations*. 2022. URL: <https://openreview.net/forum?id=kZOUYdhqkNY> (cited on page 7).
- [18] H. Goh et al. “Solving Bayesian inverse problems via variational autoencoders”. In: *Mathematical and Scientific Machine Learning*. 2022, pages 386–425 (cited on page 7).
- [19] I. Goodfellow, Y. Bengio, and A. Courville. *Deep learning*. MIT press, 2016 (cited on page 9).
- [20] I. Goodfellow et al. “Generative adversarial networks”. In: *Communications of the ACM* 63.11 (2020), pages 139–144 (cited on page 13).
- [21] E. Haber and D. Oldenburg. “A GCV based method for nonlinear ill-posed problems”. In: *Computational Geosciences* 4.1 (2000), pages 41–63 (cited on page 12).
- [22] K. Hämläinen et al. *Tomographic X-Ray Data Of A Walnut*. en. 2015. DOI: 10.5281/ZENODO.1254206. URL: <https://zenodo.org/record/1254206> (cited on pages 15, 16).
- [23] K. Hammernik et al. “Learning a variational network for reconstruction of accelerated MRI data”. In: *Magnetic Resonance in Medicine* 79.6 (2018), pages 3055–3071 (cited on page 5).
- [24] P. C. Hansen. *Discrete Inverse Problems: Insight and Algorithms*. SIAM, 2010 (cited on page 2).
- [25] P. C. Hansen, J. Jørgensen, and W. R. B. Lionheart. *Computed Tomography: Algorithms, Insight, and Just Enough Theory*. Edited by P. C. Hansen, J. Jørgensen, and W. R. B. Lionheart. Philadelphia, PA: Society for Industrial and Applied Mathematics, 2021. DOI: 10.1137/1.9781611976670. eprint: <https://epubs.siam.org/doi/pdf/10.1137/1.9781611976670>. URL: <https://epubs.siam.org/doi/abs/10.1137/1.9781611976670> (cited on page 12).

- [26] T. Hastie, R. Tibshirani, and M. Wainwright. “Statistical learning with sparsity”. In: *Monographs on statistics and applied probability* 143 (2015), page 143 (cited on page 12).
- [27] G. E. Hinton and R. R. Salakhutdinov. “Reducing the dimensionality of data with neural networks”. In: *science* 313.5786 (2006), pages 504–507 (cited on page 5).
- [28] D. P. Kingma and J. Ba. “Adam: A method for stochastic optimization”. In: *arXiv preprint arXiv:1412.6980* (2014) (cited on pages 13, 17).
- [29] D. P. Kingma and M. Welling. “Auto-encoding variational Bayes”. In: *arXiv preprint arXiv:1312.6114* (2013) (cited on pages 6, 7, 9).
- [30] D. P. Kingma, M. Welling, et al. “An introduction to variational autoencoders”. In: *Foundations and Trends® in Machine Learning* 12.4 (2019), pages 307–392 (cited on page 9).
- [31] S. Kullback and R. A. Leibler. “On information and sufficiency”. In: *The annals of mathematical statistics* 22.1 (1951), pages 79–86 (cited on page 6).
- [32] J. Lee and P. Kitanidis. “Bayesian inversion with total variation prior for discrete geologic structure identification”. In: *Water Resources Research* 49.11 (2013), pages 7658–7669 (cited on page 15).
- [33] M. Lemaire. *Structural reliability*. John Wiley & Sons, 2013 (cited on page 7).
- [34] H. Li et al. “NETT: Solving inverse problems with deep neural networks”. In: *Inverse Problems* 36.6 (2020), page 065005 (cited on pages 2, 5).
- [35] C. Lieberman and K. Willcox. “Goal-oriented inference: Approach, linear theory, and application to advection diffusion”. In: *SIAM REVIEW* 55.3 (2013), pages 493–519 (cited on pages 2–4).
- [36] C. Lieberman and K. Willcox. “Nonlinear goal-oriented Bayesian inference: application to carbon capture and storage”. In: *SIAM Journal on Scientific Computing* 36.3 (2014), B427–B449 (cited on page 2).
- [37] S. Liu and J. Zhang. “Machine-learning-based prediction of regularization parameters for seismic inverse problems”. In: *Acta Geophysica* (2021), pages 1–12 (cited on pages 2, 5).
- [38] A. Lucas et al. “Using deep neural networks for inverse problems in imaging: beyond analytical methods”. In: *IEEE Signal Processing Magazine* 35.1 (2018), pages 20–36 (cited on page 7).
- [39] J. L. Mead and R. A. Renaut. “A Newton root-finding algorithm for estimating the regularization parameter for solving ill-conditioned least squares problems”. In: *Inverse Problems* 25.2 (2008), page 025002 (cited on page 12).
- [40] A. B. Owen. *Monte Carlo theory, methods and examples*. 2013 (cited on page 18).
- [41] P. Peng, S. Jalali, and X. Yuan. “Solving inverse problems via auto-encoders”. In: *IEEE Journal on Selected Areas in Information Theory* 1.1 (2020), pages 312–323 (cited on page 7).
- [42] S. T. Radev et al. “BayesFlow: Learning complex stochastic models with invertible neural networks”. In: *IEEE transactions on neural networks and learning systems* 33.4 (2020), pages 1452–1466 (cited on page 7).
- [43] S. T. Radev et al. “JANA: Jointly Amortized Neural Approximation of Complex Bayesian Models”. In: *The 39th Conference on Uncertainty in Artificial Intelligence*. 2023. URL: <https://openreview.net/forum?id=dS3wVICqrU0> (cited on page 7).
- [44] W. Reese, A. K. Saibaba, and J. Lee. *Bayesian Level Set Approach for Inverse Problems with Piecewise Constant Reconstructions*. 2021. eprint: [arXiv:2111.15620](https://arxiv.org/abs/2111.15620) (cited on pages 15, 19).
- [45] L. I. Rudin, S. Osher, and E. Fatemi. “Nonlinear total variation based noise removal algorithms”. In: *Physica D: Nonlinear Phenomena* 60.1 (1992), pages 259–268. ISSN: 0167-2789. DOI: [https://doi.org/10.1016/0167-2789\(92\)90242-F](https://doi.org/10.1016/0167-2789(92)90242-F). URL: <https://www.sciencedirect.com/science/article/pii/016727899290242F> (cited on page 12).
- [46] L. Ruthotto, J. Chung, and M. Chung. “Optimal experimental design for inverse problems with state constraints”. In: *SIAM Journal on Scientific Computing* 40.4 (2018), B1080–B1100 (cited on page 13).

- [47] R. Salakhutdinov, A. Mnih, and G. Hinton. “Restricted Boltzmann machines for collaborative filtering”. In: *Proceedings of the 24th international conference on Machine learning*. 2007, pages 791–798 (cited on page 5).
- [48] A. Spantini et al. “Goal-oriented optimal approximations of Bayesian linear inverse problems”. In: *SIAM Journal on Scientific Computing* 39.5 (2017), S167–S196 (cited on page 2).
- [49] A. Torralba, R. Fergus, and Y. Weiss. “Small codes and large image databases for recognition”. In: *2008 IEEE Conference on Computer Vision and Pattern Recognition*. IEEE. 2008, pages 1–8 (cited on page 5).
- [50] F. Uribe et al. “A hybrid Gibbs sampler for edge-preserving tomographic reconstruction with uncertain view angles”. In: *SIAM/ASA Journal on Uncertainty Quantification* 10.3 (2022), pages 1293–1320 (cited on page 14).
- [51] C. R. Vogel. “Non-convergence of the L-curve regularization parameter selection method”. In: *Inverse Problems* 12.4 (1996), page 535 (cited on page 12).
- [52] Y. Wang, H. Yao, and S. Zhao. “Auto-encoder based dimensionality reduction”. In: *Neurocomputing* 184 (2016), pages 232–242 (cited on page 5).